

Feasibility of hydrogen production from steam reforming of biodiesel (FAME) feedstock on Ni-supported catalysts



Gaurav Nahar^{a,*}, Valerie Dupont^a, Martyn V. Twigg^b, Emiliana Dvininova^c

^a Energy Research Institute, School of Chemical and Process Engineering, The University of Leeds, LS2 9JT, UK

^b TST Ltd, Caxton, Cambridge CB23 3PQ, UK

^c MEL Chemicals, P.O. Box 6, Lumns lane, Swinton, Manchester M27 8LS, UK

ARTICLE INFO

Article history:

Received 9 September 2014

Received in revised form

17 December 2014

Accepted 21 December 2014

Keywords:

Biodiesel

Fuel cells

Hydrogen

Steam reforming

ABSTRACT

The catalytic steam reforming of biodiesel was examined over Ni-alumina and Ni-ceria-zirconia catalysts at atmospheric pressure. Effects of temperatures of biodiesel preheating/vaporising (190–365 °C) and reforming (600–800 °C), molar steam to carbon ratio ($S/C = 2-3$), and residence time in the reformer, represented by the weight hourly space velocity 'WHSV' of around 3 were examined for 2 h. Ni supported on calcium aluminate and on ceria-zirconia supports achieved steady state hydrogen product stream within 90% of the equilibrium yields, although 4% and 1% of the carbon feed had deposited on the catalysts, respectively, during the combined conditions of start-up and steady state. Addition of dopants to ceria-zirconia supported catalyst decreased the performance of the catalyst. Increase in S/C ratio had the expected positive effects of higher H_2 yield and lower carbon deposition.

© 2015 Published by Elsevier B.V.

1. Introduction

Catalytic steam reforming (CSR), partial oxidation (POX) and autothermal reforming (ATR) of natural gas are, in decreasing order of importance, the mainstream methods for hydrogen production outside of petroleum refineries. This hydrogen is then principally converted to ammonia and then to synthetic fertilizers such as urea, ammonium nitrate, and calcium ammonium nitrate. Increased need in hydrogen gas due to world population growth [1,2] resulting in higher demand in fertilizers [3], refineries [4] and clean transport fuel [5] combined with a continued pressure to reduce greenhouse gas emissions motivate research efforts into increasing the efficiency of the CSR process and using feedstocks with lower carbon footprint. In addition, reductions in environmental emissions along with higher efficiencies in comparison to internal combustion engines have resulted in considerable development in the area of fuel cells for mobile and stationary applications, with the required feedstock for mobile (PEM) fuel cells remaining high purity hydrogen gas. CSR exhibits a wide range of feedstock flexibility, providing higher yields than POX and ATR from a given feedstock due to the large water contribution to the total hydrogen produced. However the overall efficiency of the process (the

($mH_2 \cdot LHV / mFeed \cdot LHV$) for SR and ATR is in the same range. This is mainly attributed to the additional fuel demand for the burner in case of SR.

CSR can be adapted for hydrogen generation from volatile and semi volatile oxygenated hydrocarbons from biomass conversion processes. Early hydrogen production through CSR from 1st generation biofuels like sunflower, canola and rapeseed oils [6,7–9] and later, from biofuels such as the waste crude glycerol by-product of biodiesel production via transesterification of fats [10], waste or used cooking oil and palm oil fatty acid distillates [11–13], bio-oils derived from the fast pyrolysis of diverse biomass sources [14] and associated model compounds [15,16], as well as less orthodox hydrogen carriers like urea and ammonia aqueous solutions [17,18], have successfully been investigated in recent years. In contrast, hydrogen production from biodiesel is relatively new [19–22] and few catalytic [23,24] investigations have been reported. Direct utilization of biodiesel formulations in solid oxide fuel cells (SOFC) using Ni/YSZ anodes was reported by Nahar and Kendall [25] and Shitatori et al. [26]. Higher power generation using biodiesel fuelled SOFC over Ni/ScCZ anode was reported by Quang-Tuyen et al. [27] in comparison to waste cooking oil fuelled SOFC using CeO_2 -Rh anodes by Zhou et al. [28].

According to Xuan et al. [29], as biodiesel consists of shorter carbon chains in comparison to original oils it would be easier to convert to hydrogen as compared to the original oils. Further production of biodiesel is predicted to increase from 24 billion liters

* Corresponding author.

in 2011 to 42 billion liters in 2021 assuring a steady supply for the future [30]. Better handling properties of biodiesel (high calorific value and low viscosity) compared to vegetable oils could justify the use of such a refined fuel as a feedstock for hydrogen production through the CSR process. Waste cooking oil contains high amount of free fatty acids, responsible for initiating cracking reactions at the reforming temperatures leading to carbon formation and catalyst deactivation [7]. Life cycle assessment of biodiesel production using transesterification of waste cooking oil was reported to have a low carbon footprint, promoting the use of biodiesel as a hydrogen carrier [31].

Alumina supported Ni catalyst are widely used in the CSR of various hydrocarbons from methane [32] to oxygenated hydrocarbons [33] like ethanol, glycerol, vegetable oil [9], waste cooking oil [11] and bio-oil [14]. The major disadvantage of Ni based catalyst in (CSR) of hydrocarbons is carbon formation on the catalyst surface affecting the activity [34,35]. The acidic nature of alumina based catalysts has been shown to promote thermal cracking reactions in CSR of complex hydrocarbons like vegetable oil, resulting in carbon formation via aromatics and olefin production [6]. One of the approaches to reduce carbon formations is preparation of bimetallic catalyst using alkali metals like K and other metals like Sn [34], and Bi [36]. Addition of K to alumina neutralizes acidic sites of alumina thereby reducing the possibility of coke formation via cracking reactions [37]. Carbon gasification reaction is enhanced by K addition affecting carbon deposited on the catalyst surface [38]. It also increases the adsorption of steam on the catalyst surface [39] affecting steam reforming (SR) reaction (R-1). According to Trimm [34] carbide formation is an essential intermediate route to coke formation, formed by interaction of 2p carbon electrons with 3d nickel electrons. Penta-valent p metals (such as Ge, Sn and Pb or As, Sb or Bi) interact with Ni 3d electrons, reducing the chance of nickel carbide formation in turn affecting carbon formation. Pengpanich et al. [40] found that addition of Sn to NiO disrupted the active site ensembles responsible for coking. Solubility of carbon in Ni particles responsible for nickel carbide formation is also reduced by addition to Sn to Ni catalyst.

In addition to use of bimetallic catalysts, carbon formation can also be reduced by using different catalyst supports like ceria. Ceria has a unique ability to release and store oxygen (OSC) under reducing and oxidizing environments, helping to reduce carbon formation over the catalyst surface. It is shown to promote metal dispersion and activity in SR catalyst. It also exhibits superior water gas shift catalytic activity. However, ceria lacks thermal stability and undergoes sintering at high temperature, affecting OSC of the material. Ceria consists of eight oxygen cations coordinated at a corner of a cube, each anion being tetrahedrally coordinated by four cations. This makes ceria's structure more stable and prevents the conversion of Ce^{4+} to Ce^{3+} under reducing conditions. Metal decoration has been observed for metal catalysts supported on reducible oxides [41]. Deterioration of catalytic activity is also caused by decreases in metal surface area on metal supported catalysts [42]. The addition of transition metals like Zr is shown to improve the resistance of ceria to sintering [43] and enhance reducibility of ceria resulting in improved OSC of the material [44]. Additionally, the long-term thermal morphological and/or redox stability of pure ceria has been shown to be improved by the addition of Zr [45]. As a result of these improved properties of ceria–zirconia mix oxide, several Ni and noble metal supported on ceria–zirconia mix oxide, have been successfully investigated for CSR of gaseous and oxygenated hydrocarbons [46].

The aim of the present study was to optimize hydrogen production parameters using CSR of biodiesel. Effects of temperature, molar steam to carbon ratio (S/C), preheating and reforming temperatures, and reaction time represented by the weight hourly space velocity (WHSV) in the reformer on the initial performance

of the process were examined for Ni catalysts. The effect of catalyst support (alumina, calcium aluminate and ceria–zirconia) was investigated. In addition performance of bimetallic catalyst Ni–K and Ni–Sn were compared with monometallic Ni catalysts.

2. Experimental

2.1. Reactor set up

The experimental study was carried out in a packed bed reactor system as shown in Fig. 1. The reactor (R-1) consisted of a 12.7 mm (1/2-in.) o.d. and 25 cm long SS 310 stainless steel tube placed in an electric furnace (Elite thermal systems). A thermocouple (TC-4) was inserted from the bottom of the reactor by means of a Swagelok cross fitting, with side arms of the cross connecting a pressure relief valve and a condenser. The thermocouple was placed exactly below the catalyst bed. Two vaporisers (VP-1 and VP-2) for converting liquid biodiesel and water were provided. In order to limit re-condensation of biodiesel downstream of the vaporiser, the fuel vaporiser was placed exactly above the reactor while the water vaporiser was placed at an offset. Much care was also taken in minimizing the length of ducts between vaporisers and reformer so as to minimize the risk of pyrolysis of the fuel prior to reaching the reformer. The vaporisers consisted of solid cylinder heated with cartridge heaters (Elmatic Cardiff). The vaporiser for biodiesel was made of aluminum cylinder while stainless steel was used for the water. A stainless steel tube (1/4 inch o.d.) was passed through the cylinders, and vaporization occurred by indirect heating from the heated cylinder. Dual junction thermocouples (TC-1 and TC-2) were placed in both vaporization tubes to measure the temperature and provide a signal for the controllers (Watlow EZ-zone) regulating the power provided to the heaters. The vaporisers were fed with biodiesel and water by means of two syringe pumps (New Era Ltd., NE-1000) (P-1 and P-2) which were placed above them, using 25 ml SGE gas-tight glass syringes fitted with luer-locks to prevent back flow of nitrogen in the syringes. Two duct coils (special stainless steel 316, 1/4 inch o.d.) were placed around the vaporisers to use their waste heat for preheating the nitrogen gas carrier (HE-1) in the reactant mixture. The latter was used as inert diluent, through which the performing of elemental balances was made possible via a simple nitrogen balance, yielding the total dry gaseous product molar rate. This allowed process outputs of hydrogen and other products yields, as well as fuel (X_{biod}) and steam conversions ($X_{\text{H}_2\text{O}}$) to be calculated. In the equivalent real-world industrial process, nitrogen dilution would not be required. Two separate MKS mass flow controllers were used for feeding nitrogen and hydrogen, the latter being used for the pre-reduction step necessary to activate the nickel catalysts. Steam and vaporized biodiesel were mixed in a Swagelok 'tee' (MX-1) before mixing with the preheated nitrogen in a cross (MX-2) provided at the top of the reactor. A thermocouple was also inserted at this point to measure the reactor inlet temperature (TC-3). To prevent steam condensation a heating tape was provided on the pipe connecting both vaporisers from the bottom to the tee.

The product gases and condensable vapors from the reactor were passed through a condenser (HE-2) maintained at 1 °C by means of a chiller (Fisher). The condensed vapors and unreacted steam were removed and collected from a gas–liquid separator at the end of experiment. The total organic carbon (TOC) in the condensate was measured using Hach-Lang IL550 analyser. The gases collected from the top of the gas–liquid separator were passed through a silica gel drying tower (D-1) and transferred to a Varian CP-4900 micro Gas Chromatograph (GC) for analysis. The gas chromatograph was equipped with two thermal conductivity detectors. A molecular sieve 5A PLOT, 0.32 mm i.d., 10 m length column was

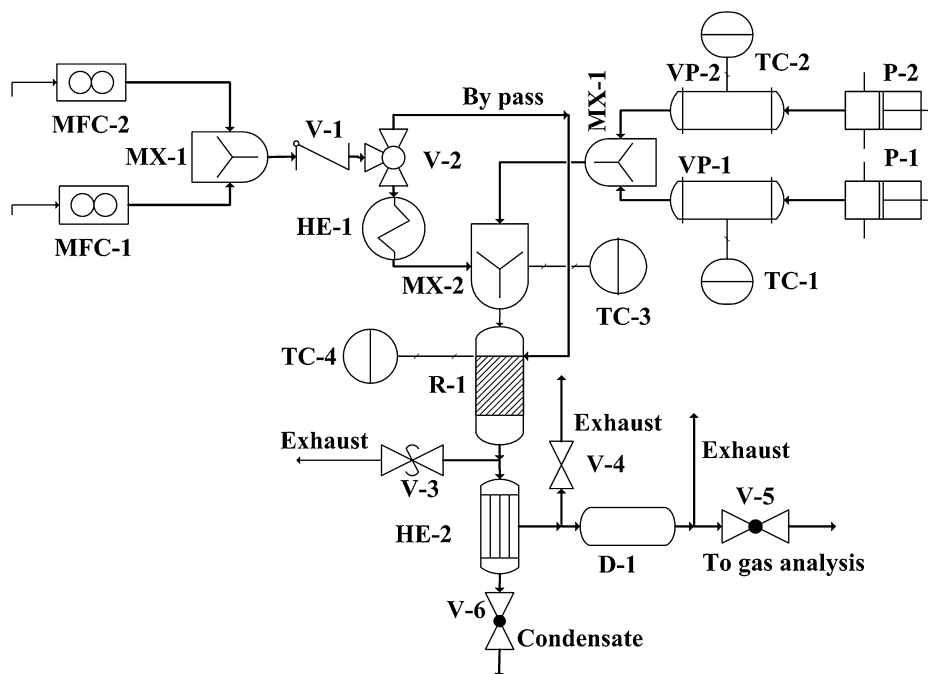


Fig. 1. Schematic of the experimental rig used in the investigation. In the figure MFC-1 and 2-mass flow controllers, V-1, 2, 3–6 valves, MX-1 mixing tee, MX-2 mixing cross, P-1 and P-2 syringe pumps, TC-1, 2–4 thermocouples, HE-1 and HE-2 heat exchangers, VP-1 and VP-2 biodiesel and water vaporisers, R-1 reactor and D-1-drying tower, respectively.

used for the analysis of hydrogen, oxygen, nitrogen, methane and carbon monoxide. Separation of alkenes like ethylene and propylene in addition to higher alkanes i.e., ethane and propane along with carbon dioxide and again, methane, was performed on a Pora-PLOT Q 0.15 mm i.d., 10 m length column.

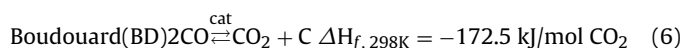
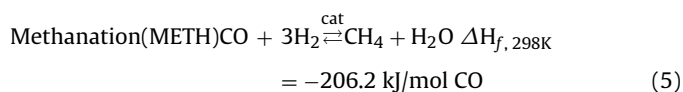
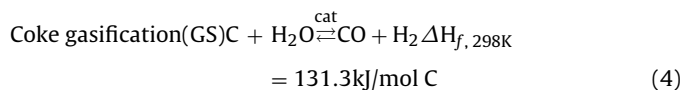
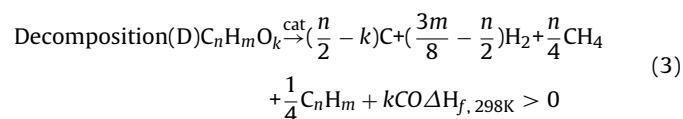
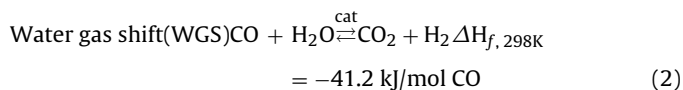
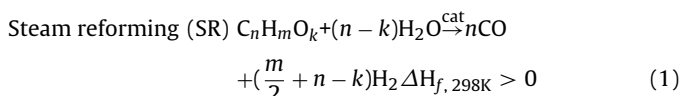
2.1.1. Test procedure

During an experiment the catalyst (pellet or powder depending on the catalyst) was sandwiched between two plugs of quartz wool (4 μ m fiber diameter) above the reactor bed thermocouple. The catalyst was reduced at the reactor operating temperature by means of 5 vol% H_2/N_2 mixture at flow rate of 200 ml/min (STP); the completion of the reduction was confirmed by steady state GC readings of H_2 . The reactor was then flushed with 180 ml/min (STP) nitrogen to remove the hydrogen used in the reduction. The vaporisers were turned on under nitrogen flow, and once the temperature set points were reached, the heating tape was turned on. Upon stabilization of the vaporisers and the heating tape set point, nitrogen flow rate was decreased to the desired flow rate and both the pumps delivering biodiesel and water were switched on.

2.1.2. Main reactions and process outputs

This section describes the main reactions involved in SR of biodiesel. It also provides the equations used to examine the performance of the process.

2.1.2.1. Reactions involved. The general SR reaction of oxygenated hydrocarbons is given by (R-1). Steam reacts with the fuel to form hydrogen and carbon monoxide. The carbon monoxide then reacts with steam to produce more hydrogen and carbon dioxide via the water gas shift reaction (R-2). Other reactions (R-3–6) can also occur during the process.



2.1.2.2. Processes output. The process performance was measured in terms of main outputs of hydrogen yield (Y_{H_2} , wt%) and hydrogen yield efficiency ($Y_{H_2, eff}$) calculated using Eqs. (i)–(ii). Fuel and steam conversions (X_{biod} and X_{H_2O}) along with selectivity to carbon containing products (S_{C-i}) and to hydrogen containing products (S_{H-i}) using Eqs. (iii)–(viii) were used to discuss the reaction mechanisms responsible for the H_2 yield results. In the equations, n , m and k are the molar numbers of carbon, hydrogen and oxygen atoms in the biodiesel of elemental formula $C_nH_mO_k$ (moisture free basis) and \dot{n} denotes a molar flow rate, e.g., $\dot{n}_{biod, in}$ and $\dot{n}_{H_2O, in}$ are the feed molar flow rates of biodiesel and water, $\dot{n}_{out, dry}$ is the molar flow rate of dry gases leaving the reactor. In addition, y_i is the dry mol fraction of gas product species i , and W_i is the molar mass of species

i. Subscripts 'exp' and 'eq' denote experimental and equilibrium calculation results, respectively, while 'in'/'out' refer to inlet/outlet conditions.

$$Y_{H_2}(\text{wt}\%) = \frac{\text{mass flow rate of } H_2 \text{ produced}}{\text{mass flow rate of biodiesel}} \times 100$$

$$= \left(\frac{W_{H_2} \times Y_{H_2} \times \dot{n}_{\text{out,dry}}}{W_{\text{biod}} \times \dot{n}_{\text{biod,in}}} \right) \times 100 \quad (\text{i})$$

$$Y_{H_2}(\text{eff}\%) = \left(\frac{Y_{H_2}^{\text{exp}}}{Y_{H_2}^{\text{eq}}} \right) \times 100 \quad (\text{ii})$$

The H_2 yield efficiency ($Y_{H_2}(\text{eff})$) calculated by (Eq. (ii)) is the ratio of the average H_2 yield during the experiments to the H_2 yield calculated at chemical equilibrium for the same conditions. Accordingly, $Y_{H_2}(\text{eff})$ values permit comparisons of catalytic activity for H_2 production by different catalysts.

The biodiesel conversion (X_{biod}) is calculated on the basis of carbon containing gas products only.

$$X_{\text{biod}} = \frac{\dot{n}_{\text{C,gas,out}}}{\dot{n}_{\text{C,in}}}$$

$$= \left(\frac{\dot{n}_{\text{out,dry}}(Y_{\text{CO}} + Y_{\text{CO}_2} + Y_{\text{CH}_4} + 2Y_{\text{C}_2\text{H}_4} + 2Y_{\text{C}_2\text{H}_6} + 3Y_{\text{C}_3\text{H}_6} + 3Y_{\text{C}_3\text{H}_8})}{n \times \dot{n}_{\text{biod,in}}} \right) \times 100 \quad (\text{iii})$$

Full carbon balance is then derived over the period of the experiments (2 h). It comprised of carbon accumulated on the catalyst surface, in addition to the carbon collected in the condensates (measured by CHN–O analysis) and the carbon leaving with the gases. The carbon leaving with the three streams collectively accounts to 'C out', in moles, compared to the moles of C in the biodiesel feed ('C in'). An elemental analyser (Flash EA2000 by CE Instruments) was used to determine the C, H, N and O (CHN–O) on the catalyst. Closeness to carbon closure was expressed in % by $100 \times (1 - \text{C out/C in})$ in tables, with small values (<5%) representing good closure.

The steam conversion (X_{H_2O}) is derived from a hydrogen balance, i.e. the molar flow of water consumed equals the molar flow of (2H) contained in all the gases minus the molar flow of (2H) contained in the converted biodiesel; this neglects the hydrogen that may have been present on the coked catalyst or in the condensates.

$$X_{H_2O} = \left(\frac{\dot{n}_{H_2O,\text{in}} - \dot{n}_{H_2O,\text{out}}}{\dot{n}_{H_2O,\text{in}}} \right) \times 100$$

$$\approx \left(\frac{\dot{n}_{(2H \text{ in gas products})} - \dot{n}_{(2H \text{ in converted biodiesel})}}{\dot{n}_{H_2O,\text{in}}} \right) \times 100 \quad (\text{iv})$$

$$X_{H_2O}$$

$$\approx \left(\frac{\dot{n}_{\text{out,dry}}(Y_{H_2} + 2Y_{CH_4} + 2Y_{C_2H_4} + 2Y_{C_2H_6} + 3Y_{C_3H_6} + 4Y_{C_3H_8}) - 0.5mX_{\text{biod}}\dot{n}_{\text{biod}}}{\dot{n}_{H_2O,\text{in}}} \right) \times 100 \quad (\text{v})$$

Steam conversion efficiency ($H_2O \text{ conv}(\text{eff})$) uses the same definition as for the H_2 yield efficiency, i.e., it is the ratio of average steam conversion obtained during the experiments ($X_{H_2O}^{\text{exp}}$) to the steam conversion calculated at chemical equilibrium ($X_{H_2O}^{\text{eq}}$) and allows comparison of catalysts' activity.

$$H_2O \text{ conv}(\text{eff}\%) = \left(\frac{X_{H_2O}^{\text{exp}}}{X_{H_2O}^{\text{eq}}} \right) \times 100 \quad (\text{vi})$$

Selectivity to hydrogen containing gas products is a simple ratio of the dry mol fraction of the product of interest (i.e., H_2 , CH_4 , C_2H_6 , C_2H_4 , C_3H_6 or C_3H_8) divided by the sum of all of them.

$$S_{H-H_2} = \left(\frac{Y_{H_2}}{Y_{H_2} + Y_{CH_4} + Y_{C_2H_4} + Y_{C_2H_6} + Y_{C_3H_6} + Y_{C_3H_8}} \right) \times 100 \quad (\text{vii})$$

Selectivity to carbon containing gas products is calculated in a similar way:

$$S_{C-CO} = \left(\frac{Y_{CO}}{Y_{CO} + Y_{CO_2} + Y_{CH_4} + Y_{C_2H_4} + Y_{C_2H_6} + Y_{C_3H_6} + Y_{C_3H_8}} \right) \times 100 \quad (\text{viii})$$

Thus methane and the higher gaseous hydrocarbons have two types of gas product selectivity: hydrogen containing, e.g., S_{H-H_2} – $C H_4$, and carbon containing, e.g., $S_{C-C H_4}$.

The basic thermal efficiency of the global reaction of SR of biodiesel is evaluated using Eq. (ix).

$$\text{Reforming}(\text{eff}\%) = \left(\frac{\dot{n}_{H_2} \times \text{LHV}_{H_2}}{\dot{n}_{\text{biod,in}} \times \text{LHV}_{\text{biod}}} \right) \times 100 \quad (\text{ix})$$

In Eq. (ix), LHV refers to the lower heating values of hydrogen and biodiesel in kJ/mol. The LHV of biodiesel used was 37.5 kJ/mol.

The thermodynamic equilibrium calculations for comparison with experiments were performed using a Gibbs free energy minimization method using the chemical equilibrium and applications (CEA) software provided by NASA. The thermodynamic properties for methyl esters were obtained from Osmont et al. [47].

2.2. Catalyst preparation

A 17 wt% cerium doped zirconia oxide ($\text{Ce}_{0.12}\text{Zr}_{0.88}\text{O}_2$) and hydroxide supplied by MEL chemicals, UK, were utilized in catalyst preparation. The hydroxide material to be used as a support was initially calcined at 600 °C for 6 h, while the oxide was pre-calcined by the manufacturer. Nickel supported on ceria–zirconia (calcined in-house) was prepared using wet and dry impregnation methods. In the case of the wet impregnation method, the calculated quantity of nickel nitrate was dissolved in 50 ml water and the calcined support was added to the solution and stirred for three hours, with the wet material dried overnight in an oven at 120 °C and calcined at 600 °C for 6 h. In the dry impregnation method, the calculated amount of nitrate salt was added to 50 ml water that was added dropwise to the catalyst support via a burette. Once a paste was formed the addition was stopped and the material was dried over a hot plate to evaporate the water; this procedure was repeated until all the solution had been added and the material was dry. The drying procedure was performed 4–5 times. The solid was then calcined using the same methodology (600 °C for 6 h). The pre-calcined oxide supplied by the manufacturer was used in the preparation of 10 wt% Ni and 10 wt% Ni doped with 2 wt% K and 2 wt% Sn using the described wet impregnation method. This loading of NiO was chosen based on XRD and surface area results of a range of loadings (10–30 wt%). The 10 wt% NiO loaded catalyst showed highest surface and smallest crystallite size (Table 2). The results for 20–30 wt% NiO loaded catalyst are not shown here.

Two catalysts supplied by industrial collaborators were also tested. One was 18 wt% NiO supported on α -alumina provided by Johnson Matthey Plc and the other was a 15 wt% Ni supported on calcium aluminate provided by TST Ltd. The 18 wt% NiO supported on α -alumina was tested as received after particle size reduction. The same catalyst was also tested after doping with K using the wet impregnation method to obtain a 18 wt% NiO/1.67 wt% K, supported on α -alumina. These catalysts were in pellet form and were crushed to obtain particles 0.85–2 mm. These particle sizes were selected to prevent diffusion limitations [14].

The 18 wt% Ni supported on α - Al_2O_3 and 1.67 wt% K doped 18 wt% Ni supported on α - Al_2O_3 catalyst henceforth will be represented by 'Ni/Al' and 'Ni–K/Al' in the paper. Similarly 10 wt% Ni,

2 wt% K and Sn doped 10 wt% Ni supported on $\text{Ce}_{0.12}\text{Zr}_{0.88}\text{O}_2$ will be represented by Ni/Ce–Zr, Ni–K/Ce–Zr and Ni–Sn/Ce–Zr, respectively. Nickel supported calcium aluminate will be represented by Ni/Ca–Al.

2.3. Characterization of biodiesel and catalysts

Elemental CHN–O analysis of the biodiesel sample was performed using an Elemental Analyser (Flash EA2000 by CE Instruments). CHN–O was also used to determine the carbon content on the catalyst after use, and in the condensates collected during experiments. Proximate analysis of the biodiesel samples was performed by thermo-gravimetry using a TGH1000 (Stanton Redcroft). A 180 mg biodiesel sample was subjected to heating at 5 °C/min from ambient to 400 °C with 50 ml/min of nitrogen followed by 25 °C/min from 400 °C to 900 °C under same nitrogen flow. Finally 50 ml/min of air was introduced at 900 °C and the sample was held for 10 min. Calorific value of the biodiesel was obtained using bomb calorimetry (Parr Instruments model-6200). The acid value determination of the biodiesel was performed using British Standard EN14104 (2003) method. The biodiesel's composition in fatty acid methyl esters was obtained by means of gas chromatograph (Clarus 500, PerkinElmer) fitted with flame ionization detector, using a 100 m long, 0.25 mm i.d. and 0.25 μm film thickness, fused silica column (SUPELCO SPTM 2380).

Catalysts were characterized by powder X-ray diffraction (XRD) using a Bruker D8 instrument by means of X Cu K α radiation. Phase analysis based on the XRD data was obtained using the X'Pert High Score Plus software. Rietveld refinement was used to measure the phase compositions of NiO, Al_2O_3 and Ce–Zr as well as the crystallite sizes (Scherrer equation accounting for peak broadening by instrument and strain) [48]. The dispersion of Ni on the catalyst was calculated using (Eq. (x)), assuming that all particles were identical spheres.

$$D(\%) = \left(\frac{fA}{\rho \sigma N_A} \right) \times \left(\frac{S}{V} \right) \times 100 \quad (\text{x})$$

In (Eq. (x)), A is the atomic weight of Ni (58.6 g mol^{−1}), ρ the specific mass (or density) of Ni is 8.9×10^{-21} g nm^{−3}, σ is the average surface area occupied by one Ni atom at the surface, which was assumed to be 0.065 nm². N_A is the Avogadro's number (6.022×10^{23} mol^{−1}). S/V is the surface area to volume ratio and f is the fraction of surface of the active phase which is effectively exposed to the reactants (biodiesel and steam) during the CSR reaction. It was assumed that $f = 1$ and S/V for spherical particles was calculated to $6/d$, where d is the crystallite size of Ni in nm, obtained from XRD.

Surface area, pore-size and pore-volume analysis of the catalysts were obtained using Quantachrome Nova 2200 surface area analyzer, using nitrogen adsorption. The samples were vacuum out-gassed at 300 °C for 3 h before the analysis was carried out. The SEM imaging of the used catalyst was used to observe carbon formation on the catalyst surface with a Hitachi SU8230. The EDX analysis of the samples was performed using an INCA 350 EDX system fitted with an 80 mm² X-Max SDD detector, Oxford Instruments. The chemical characterization of all the samples was conducted by using INCA and Aztec software supplied by Oxford Instruments. The samples were prepared a day before the analysis. The samples were suspended in methanol and were placed on the stubs. The methanol was evaporated and the sample was decontaminated in an ozone treatment chamber to remove unwanted hydrocarbons from the sample. The treated sample was stored in vacuum in the same chamber prior to analysis.

Table 1

Ultimate and proximate analyses of the biodiesel, and chemical composition by gas chromatography.

Ultimate and proximate analysis		Esters	(wt.%)
Cwt.(%)	75.35	Methyl laurate (C13(0))	0.09
Hwt.(%)	13.53	Methyl myristate (C15(0))	0.33
Owt.(%)	11.10	Methyl palmitate (C17(0))	16.86
Volatile wt.(%)	99.63	Methyl palmitoleate (C17(1))	0.34
Carbon residues wt.(%)	0.28	Methyl stearate (C19(0))	3.88
Ash wt.(%)	0.10	Methyl oleate (C19(1))	51.34
Calorific value (MJ/kg)	37.5	Methyl linoleate (C19(2))	21.29
Acid value (mg KOH/g)	0.92	Methyl linolenate (C19(3))	1.69
Free fatty acid wt.(%)	0.46	Methyl arachidate (C20(0))	0.56
		Methyl gadoleate (C21(1))	0.90
		Methyl behenate (C23(0))	0.16
		Methyl erucate (C23(1))	0.43
		Methyl lignocerate (C25(0))	0.16
		Unknown	1.96

3. Results and discussion

3.1. Characterization of biodiesel

According to the results of the proximate analysis shown in Table 1, more than 99.5 wt% of the biodiesel consisted of volatile organic compounds, with minimum amount of carbon residue and ash content of less than 0.1 wt% (Table 1). Most of the volatiles were released between 190 and 400 °C. This would have allowed complete vaporization of the reforming feedstock at relatively low temperatures for optimum reaction conditions between the feedstock and steam over the catalyst bed. Gas chromatography determined the biodiesel consisted mainly of methyl oleate (51 wt%), methyl linoleate (21 wt%), methyl palmitate (17 wt%) and methyl stearate (4 wt%), as shown in Table 1.

The elemental molar composition derived for this biodiesel based on the ultimate analysis was $\text{C}_{18.07}\text{H}_{38.59}\text{O}_2$, which was used in performing the elemental balances for the experimental outputs Eqs. (i)–(viii). With this formula the maximum theoretical H_2 yield (not taking into account equilibrium limitations) would have been 37.5 wt%, corresponding to complete conversion to CO_2 and H_2 . However, using the composition derived by GC analysis and neglecting the unknown 1.96 wt% content listed in Table 4, the elemental formula for the FAMES mixture became $\text{C}_{18.07}\text{H}_{38.59}\text{O}_2$, in slight discrepancy with the formula derived from the ultimate analysis. The GC-derived biodiesel formula of $\text{C}_{18.75}\text{H}_{35.34}\text{O}_2$ corresponded to a maximum theoretical H_2 yield of 36.7 wt%. On this basis, it is fair to estimate that the maximum theoretical H_2 yield was ca. 37 wt%. The stoichiometric molar steam to carbon ratio (S/C) for complete SR of the biodiesel to CO_2 and H_2 products was 1.9. The GC composition was used as basis to determine, the molar input for performing the chemical equilibrium calculations using CEA. Equilibrium H_2 yield as well as biodiesel and steam conversions represent the actual maximum values that the experimental H_2 yield, biodiesel (X_{biod}) and steam conversion ($X_{\text{H}_2\text{O}}$) can take at given temperature, pressure and feed flow rates.

3.2. Catalyst characterization

The characterization of the fresh and used Ceria–zirconia – and Al_2O_3 supported – catalysts is discussed in this section. The X-ray diffraction data for the Ni/Ca–Al catalyst is not provided as the catalyst contained large amount of amorphous material making it difficult to perform Rietveld refinement.

3.2.1. Powder X-ray diffraction

3.2.1.1. Fresh catalysts. Table 2 lists the characteristics of the fresh and used Ce–Zr supported catalysts prepared using impregnation

Table 2

XRD and BET analyses of fresh and used Ce–Zr supported nickel catalysts prepared using impregnation method.

Catalyst/Support	BET(m ² /g)	Cryst. size (nm)	Pore size(nm)	PoreVol.(cm ³ /g)	Ni Disp (%)	Ce-Zr(wt%)	NiO or Ni (wt %)
		Ce-Zr	NiO/Ni				
Fresh							
In house calcined Ce–Zr	60.35	11.22	–	6.03	0.18	–	–
pre-calcined Ce–Zr	101.46	11.55	–	4.73	0.22	–	–
NiO/Ce–Zr ^a	59.70	11.41	15.49	4.69	0.13	6.35	90.50
NiO/Ce–Zr ^b	66.59	11.62	23.98	4.73	0.14	4.22	9.70
NiO/Ce–Zr ^c	88.78	11.92	13.59	3.58	0.18	7.47	90.52
NiO–K ₂ O/Ce–Zr ^c	60.88	12.19	13.54	6.08	0.17	6.72	90.13
NiO–SnO/Ce–Zr ^c	63.59	11.38	13.74	4.68	0.16	7.22	90.25
Used							
Ni/Ce–Zr ^{c,d}	60.49	12.67	12.72	6.04	0.19	7.95	93.38
Ni–K/Ce–Zr ^{c,d}	27.86	12.67	16.94	11.61	0.12	5.97	91.35
Ni–Sn/Ce–Zr ^{c,d}	59.66	12.62	11.79	6.04	0.21	8.57	90.73

^a Catalyst prepared using wet impregnation of in-house calcined Ce–Zr support.^b Catalyst prepared using dry impregnation of in-house calcined Ce–Zr support.^c Catalysts prepared using wet impregnation of pre-calcined Ce–Zr support.^d The catalyst performance was evaluated at 650 °C, using S/C of 3 and WHSV of 3.18 h^{−1} with vaporiser temperatures of 190 and 170 °C for biodiesel and water, respectively. The tested catalyst were prepared using wet impregnation of pre-calcined Ce–Zr support.**Table 3**As Table 2 for the Al₂O₃ supported catalysts.

Catalyst	BET (m ² /g)	ReactorT (°C)	VaporiserT (°C)	WHSV(h ^{−1})	NiO or Ni (wt. %)	Al ₂ O ₃ (wt.%)	NiO or NiCryst. size (nm)
Fresh							
NiO/Al	5.71	–	–	–	17.7	82.3	47.9
NiO–K ₂ O/Al	2.27	–	–	–	18	82	34.69
NiO/Ca–Al	33.59	–	–	–	–	–	–
Used							
Ni/Al	–	600	365	3.52	13.8	86.2	30.91
Ni/Al	3.83	650	365	3.52	13.8	86.2	34.91
Ni/Al	4.71	700	365	3.52	13.9	86.1	31.87
Ni/Al	2.21	800	365	3.52	13.7	86.3	38.13
Ni/Al	3.39	650	190	3.18	13.7	86.3	31.06
Ni–K/Al	2.02	650	190	3.18	15.7	84.3	37.79
Ni/Ca–Al	21.30	650	190	3.18	–	–	–

methods. Phase compositions and crystallite sizes were derived from performing Rietveld refinement on the XRD spectra. Fig. 2a shows the XRD spectra for the catalysts prepared using wet impregnation and dry impregnation methods on the in-house calcined Ce–Zr support. Fig. 2b corresponds to the XRD spectra of the catalysts prepared utilizing wet impregnation method on the pre-calcined Ce–Zr support supplied by MEL chemicals, UK.

The diffraction peaks for Ce–Zr were observed at 2θ of 29, 35, 49, 59, 81 and 94°, respectively, with highest intensity peak at 29°. A cubic crystal system with tetragonal crystalline structure was observed. Absence of peaks responsible for pure ZrO₂ at 51° (220) and 61° (311) suggested the existence of a homogeneous solid solution of Ce–Zr and complete incorporation of Zr in the cerium crystal structure. Both the bare supports i.e., pre- and in-house calcined supports (Fig. 2b) yielded identical data, inferring that both supports consisted of the same components i.e., Ce–Zr mix oxide; therefore the in-house calcination of the cerium–zirconium hydroxide resulted in the complete formation of Ce–Zr mix oxide. The 2θ values of 37, 43 62–63, 75 and 79° shown in Fig. 2a–c are attributed to the diffraction of NiO in the sample [49].

The crystallite size of Ce–Zr remained constant throughout: ~11.5 nm. The method of preparation had a significant effect on the NiO crystallite sizes, with the wet impregnation method resulting in significantly lower size as compared to the dry impregnation method (15.5 vs. 24 nm). The NiO crystallite size of the catalyst prepared using wet impregnation of the pre-calcined Ce–Zr was slightly smaller than that of the in-house calcined Ce–Zr support (13.5 vs. 15.5 nm) but not significantly so. The dispersion of NiO was affected by the crystallite size, with catalyst prepared by wet impregnation of pre-calcined Ce–Zr showing highest dispersion. The NiO oxide crystallite sizes in the fresh Ni/Ce–Zr, Ni–K/Ce–Zr and

Ni–Sn/Ce–Zr catalysts prepared using pre-calcined Ce–Zr support were very similar (Table 2), resulting in similar dispersion values.

But small amount of micro strain was observed in case of the doped fresh Ni–K and Ni–Sn catalysts. Peaks attributed to K₂O and SnO were not observed suggesting fine dispersion of the dopants on Ce–Zr and hence they were not detected by XRD. Pengpanich et al. [40] reported similar results in the case of Ni–Sn/Ce–Zr catalysts utilized in partial oxidation of iso-octane. The existence of peaks attributable to single-phase Ni₃Sn, Ni₃Sn₂ and Ni₃Sn₄ were not detected either in the present Ni–Sn/Ce–Zr catalysts.

Similarly to Table 2 for the Ce–Zr catalysts, Table 3 lists the characteristics of the fresh and used Al₂O₃ supported catalysts. Fig. 2c shows the XRD spectra for fresh Ni/Al and Ni–K/Al catalysts. The 2θ values of 25, 35–37, 43 and 52–57° are attributed to Al₂O₃ in the catalyst with highest intensity peak occurring at 43°. Addition of K to fresh Ni/Al catalyst was shown to reduce significantly NiO crystallite size (from 48 to 35 nm). Higher micro strain was observed in case of Ni–K/Al catalyst in comparison to bare Ni/Al catalyst. Like the Ni–K/Ce–Zr catalyst, no peaks for K₂O were observed in fresh Ni–K/Al catalyst. In dry reforming of propane using Mo–Ni/γ–Al₂O₃ catalyst, Siahvashi and Adensia [50] reported that K₂O was finely dispersed over Mo–Ni/γ–Al₂O₃ catalyst and could not be detected by XRD. The Rietveld refinement allowed to derive 17.7 and 18 wt% for NiO content in the case of the fresh Ni/Al and Ni–K/Al catalysts, respectively.

3.2.1.2. Used catalysts. Fig. 3a and b shows the XRD spectra for the used Al₂O₃ and Ce–Zr supported catalysts, respectively. Peaks attributed to Ni were observed at 2θ values of 44, 51, 76 and 91, with highest intensity displayed at 44°. No peaks pertaining to NiO were observed in any of the catalysts, indicating effective

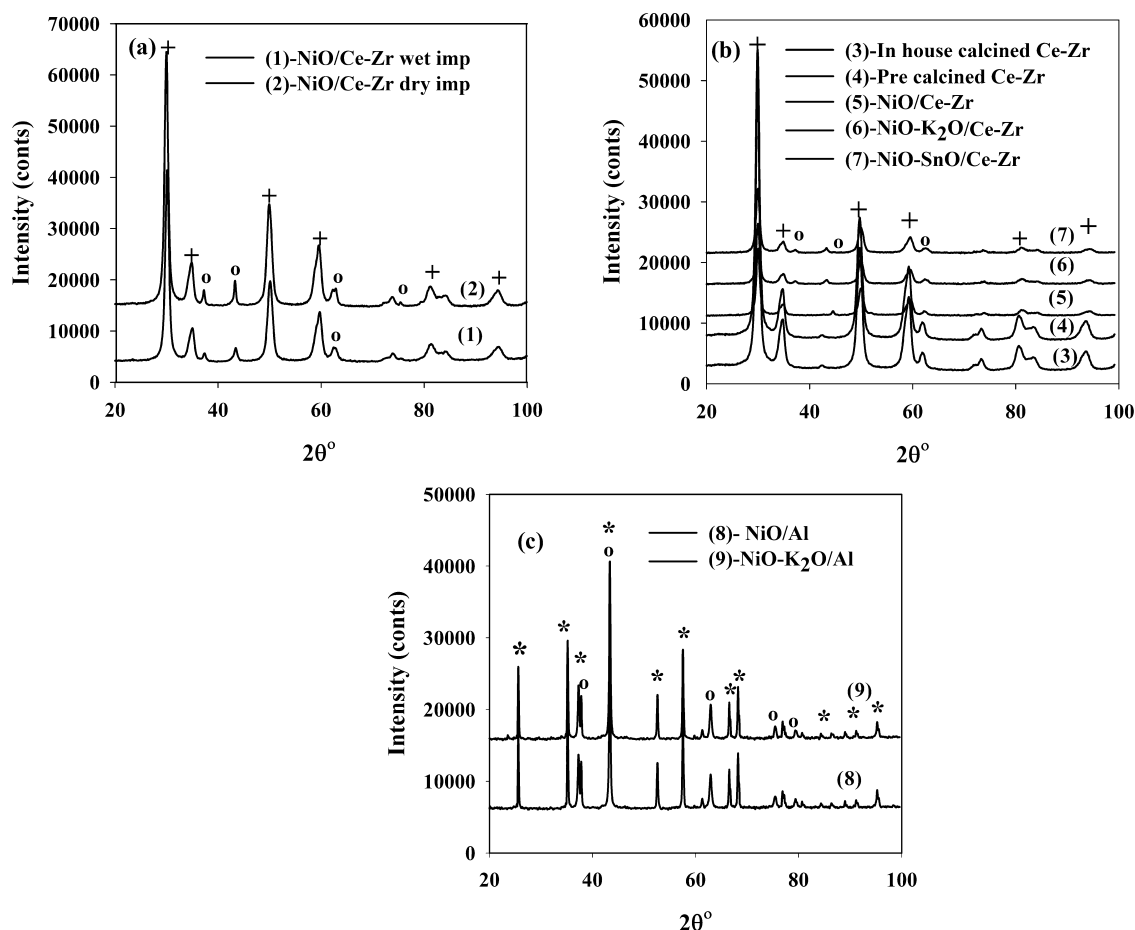


Fig. 2. X ray diffraction patterns for fresh Ni catalysts. (a) Ni catalysts prepared using wet and dry impregnation of in-house calcined Ce-Zr support, (b) Ni catalysts supported on pre-calcined Ce-Zr support, and 2(c) fresh Ni/Al and Ni-K/Al catalysts. NiO oxide peaks are marked by (o), while (+) and (*) are peaks of Ce-Zr and Al supports.

reduction during the H₂ flow pre-treatment and no deactivation of the catalyst by re-oxidation during their use. Phase composition and crystal sizes for the used Ni/Al catalysts are included in Table 3. The average Ni content of the used Al₂O₃-supported catalyst was around 13.8 wt% compared to the expected value of 14.5 wt% calculated from fully reducing the 17.7 wt% NiO of the fresh, oxidized catalyst. This would suggest that a small amount of Ni may have corroded from the catalyst and was carried out of the reactor into the condensate similarly to [51]. The Ni crystallite sizes of the Al₂O₃-supported catalyst increased slightly with temperature as expected by sintering of Ni (from 31 at 600 °C to 38 nm at 800 °C in Table 3).

After use, Ni-K and Ni-Sn catalyst exhibited higher Ni content as compared to bare Ni/Ce-Zr catalyst. The Ni content in Ni-Sn/Ce-Zr catalyst was 9.2 wt% in comparison to 6.2 and 8.6 wt% in Ni/Ce-Zr and Ni-K/Ce-Zr catalyst. The Ni crystallite size of the used Ni-K/Ce-Zr catalyst was higher as compared to Ni/Ce-Zr and Ni-Sn/Ce-Zr catalysts.

3.2.2. Surface area and pore structure

Representative nitrogen adsorption-desorption isotherms of the wet and dry impregnated NiO supported on in-house calcined Ce-Zr oxide with their BJH (Barrett-Joyner-Halenda)

Table 4
Carbon balance of CSR of biodiesel based on total input mol of C ($C_{in} = 1.08 \times 10^{-1}$ mol) over duration of experiment (7200 s), with output (C_{out}) consisting of mol C converted to gases, volatiles in the condensate and deposited on catalyst. All experiments at S/C of 3 except one (* S/C = 2). 'Vprsr' is 'vaporiser'.

Catalyst	Reactor <i>T</i> (°C)	Vprsr <i>T</i> (°C)	WHSV (h ⁻¹)	100 × [1 - (C_{out}/C_{in})] %	Carbon on catalyst		Carbon in condensate		Carbon in gases	
					Mol	% C out	Mol	% C out	Mol	% C out
Ni/Al	600	365	3.52	6.2	1.7E-02	16.3	7.2E-04	0.2	8.5E-02	83.5
Ni/Al	650	365	3.52	13.2	4.0E-03	4.3	1.9E-04	0.2	9.0E-02	95.5
Ni/Al	700	365	3.52	0.4	7.6E-03	7.0	3.6E-05	0.0	1.0E-01	92.9
Ni/Al	800	365	3.52	11.9	1.7E-03	1.8	3.3E-05	0.0	9.3E-02	98.2
Ni/Al	650	190	3.18	10.6	4.0E-03	4.2	7.7E-05	0.1	9.3E-02	95.6
Ni-K/Al	650	190	3.18	15.7	3.3E-03	3.6	5.5E-05	0.1	8.8E-02	96.3
Ni/Ca-Al	650	190	3.52	7.0	6.0E-03	6.2	2.1E-04	0.2	9.4E-02	93.6
Ni/Ca-Al	650	190	3.18	0.1	3.7E-03	3.5	2.5E-05	0.0	1.0E-01	96.4
Ni/Ca-Al	650	190	2.85	11.6	2.7E-03	2.8	1.5E-05	0.0	9.3E-02	97.1
Ni/Ca-Al*	650	190	3.18	7.1	7.3E-03	7.3	0.0E+0	0.0	9.3E-02	92.7
Ni/Ce-Zr	650	190	3.18	2.4	1.4E-03	1.3	2.6E-04	0.2	1.0E-01	98.5
Ni-K/Ce-Zr	650	190	3.18	3.9	6.5E-03	6.3	4.3E-05	0.0	9.7E-02	93.7
Ni-Sn/Ce-Zr	650	190	3.18	7.0	3.0E-03	3.0	1.5E-04	0.0	9.7E-02	97.0

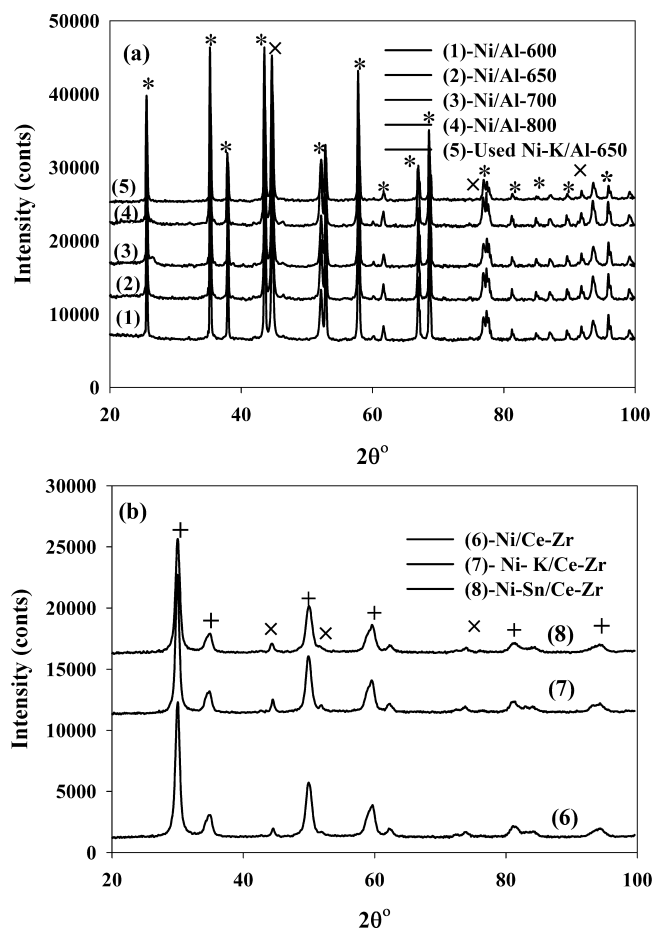


Fig. 3. X ray diffraction patterns for used (a) Al_2O_3 and (b) Ce–Zr (pre-calcined) supported catalysts. Ni peaks are marked with (x) and Ce–Zr and Al supports are marked by (+) and (*).

pore size distribution of the corresponding samples are shown Supplement 1. The adsorption–desorption isotherms of wet impregnated Ni, Ni–K and Ni–Sn catalyst supported on pre-calcined Ce–Zr support with their respective BJH pore size distributions of these catalysts are shown in Supplement 2. The surface area, pore size and pore volume results for the fresh and used catalysts prepared using in-house calcined and pre-calcined Ce–Zr supports are listed in Table 2. The surface area of fresh and used Ni/Al and Ni/Ca–Al catalysts is documented in Table 3.

See Excel sheet 1 as supplementary file. Supplementary material related to this article found, in the online version, at <http://dx.doi.org/10.1016/j.apcatb.2014.12.010>.

See Excel sheet 1 as supplementary file. Supplementary material related to this article found, in the online version, at <http://dx.doi.org/10.1016/j.apcatb.2014.12.010>.

The isotherm for all the Ce–Zr supported catalysts can be attributed to type IV and exhibits type H_1 hysteresis, which presents the typical characteristic of capillary condensation in mesoporous (between 2 and 50 nm) and contains either ink bottle or trough shaped pores. Chen et al. [52] and Aasberg-Petersen [53] reported similar observations for Al_2O_3 and silica modified Ce–Zr oxides. In the case of surfactant assisted preparation of 5 wt% Ni/Ce_{0.6}Zr_{0.4}O₂ catalyst, Sukonket et al. [54] reported the existence of type IV isotherm exhibiting H_2 hysteresis. The surface area of the pre-calcined support was 68% higher than the in-house calcined support (101 vs. 60 m²/g). This suggests that the in-house calcination processes were less homogeneous compared to those employed by the manufacturer. The surface area obtained with

the dry impregnation method was slightly higher than with the wet impregnation method for the in-house calcined Ce–Zr support (67 vs. 60 m²/g). On the other hand, the fresh Ni/Ce–Zr catalyst prepared with the pre-calcined support exhibited the highest surface area (89 m²/g), compared to those prepared using in-house calcined support. The addition of dopants to Ni/Ce–Zr catalyst decreased appreciably the surface area of the pre-calcined supported catalyst (61–64 m²/g from 89 m²/g). The surface area of the Al_2O_3 supported catalysts (Ni/Al and Ni/K–Al) was considerably less as compared to Ca–Al and Ce–Zr ones. Surface areas of 5.7 and 2.3 m²/g were noted for fresh Ni/Al and Ni/K–Al catalysts (Table 3). Fresh Ni/Ca–Al exhibited a surface area of 33 m²/g.

The nitrogen adsorption–desorption isotherms of the used Ni, Ni–K and Ni–Sn catalyst supported on pre-calcined Ce–Zr are represented in Supplement 3. After use, the surface area of the undoped catalyst decreased from 88 to 60 m²/g, suggesting a substantial sintering of the catalyst. This was observed through SEM analysis of the sample. Fig. 4 shows a SEM image of the used Ni/Ce–Zr catalyst. The presence of small cluster of Ni crystallites was observed around the support (Fig. 4). This was confirmed by EDX spectra of the clusters revealed by high Ni intensity in the examined spectra.

See Excel sheet 1 as supplementary file. Supplementary material related to this article found, in the online version, at <http://dx.doi.org/10.1016/j.apcatb.2014.12.010>.

The highest surface area decrease was observed for the K-doped catalyst, for which a 56% decrease was observed (28 m²/g vs. 61 m²/g). In contrast with the undoped Ni and the Ni–K catalysts, the Ni–Sn catalyst exhibited very small decrease in surface area (59 m²/g vs. 63 m²/g). Surface area of the Ni/Al catalysts decreased with rise in temperature (Table 3). Highest reduction in the surface area with Ni/Al catalyst was observed in the evaluation performed using 800 °C as the reactor operation temperature. As compared to the fresh catalyst, 61% reduction in the surface area of the Ni/Al catalyst was recorded at 800 °C (2.2 m²/g vs. 5.7 m²/g). This suggests that Ni/Al catalyst evaluated at 800 °C underwent significant amount of sintering. The Ni/Ca–Al catalyst also exhibited reduction in surface area similar to Ni/Ce–Zr catalyst. After use, the surface area of the catalyst reduced from 33 to 21 m²/g. Among the Al_2O_3 based catalysts Ni–K/Al catalyst exhibited negligible decrease in surface area, this was small to start with (2.0 m²/g vs. 2.2 m²/g).

3.3. Catalyst performance evaluation

The catalytic performance of the biodiesel SR was evaluated using a biodiesel flow rate of 0.978 ml/h and varying steam flow rate between 1.95 ml/h and 2.92 ml/h based on intended molar steam to carbon ratio. Nitrogen flow rate was varied from 50 to 30 ml/min to adjust the WHSV (weight hourly space velocity = ratio of total feed mass flow rate, including N_2 , to catalyst mass).

3.3.1. Effect of temperature

The Ni/Al catalyst was selected to determine the effect of temperature on the performance of the process. This was evaluated using biodiesel liquid flow rate of 0.978 ml/h (20 °C) and liquid water flow of 2.92 ml/h (20 °C), resulting in a molar steam to carbon ratio of 3, with nitrogen gas flow rate of 50 ml/min (STP), using 365 °C and 170 °C vaporiser temperatures for biodiesel and water, respectively. The biodiesel flow rate accounted for a carbon feed rate of $1.50 \times 10^{-5} \text{ mol s}^{-1}$ for all the experiments, which is used to perform the carbon balance over the initial 7200 s of steady state.

As seen in Table 1, the biodiesel tested mainly consisted of a mixture of fatty acid methyl esters of 19 carbon length (77.7 wt% of combined oleate, linoleate and stearate) with smaller amounts of C_{17} (16.9 wt% palmitate), 1.5 wt% C_{21} (arachidate and gadoleate) and 0.59 wt% C_{23} . It is unlikely that the SR reaction (R-1) involves the direct reaction of steam with these very long molecules to

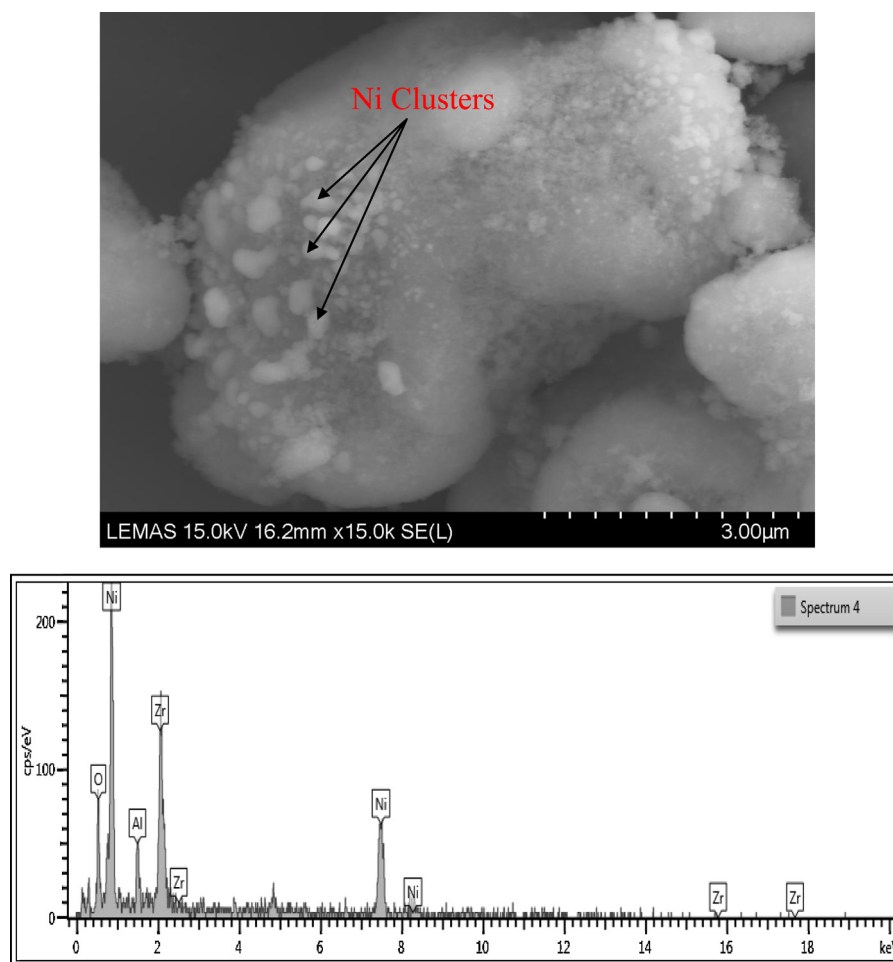


Fig. 4. The SEM image used Ni/Ce-Zr catalyst at 15 K mag with the EDX spectra. The catalyst was tested in CSR of biodiesel at S/C of 3 with reactor temperature of 650 °C and WHSV of 3.18 h⁻¹.

produce CO and H₂. Instead, it is expected that the FAMES first break up into smaller fragments under thermal and catalytic effects (catalytic cracking) and that the smaller fragments then undergo SR, similarly to what Marquievich et al. [6] proposed for vegetable oil feedstock.

The effect of temperature on the main process outputs of CSR of biodiesel is shown in Fig. 5 which contains the hydrogen data (H₂ yield, H₂ yield efficiency (eff), and selectivity (S_{H-H₂}) and process efficiencies (H₂O conv (eff), Reforming (eff)).

Hydrogen yield efficiencies of ca. 80% were found at all temperatures in the range (600–800 °C) except 700 °C where a peak to 87% was recorded, evidencing conditions not quite at, but closest to equilibrium. The decrease in yield above 700 °C would be as a result of sintering of the catalyst (Table 3), resulted in lower yield efficiency. This is evident from slight increase in methane selectivity. Methane selectivity increased from 0.1 to 0.5% with increase in temperature from 700 to 800 °C. The efficiencies corresponded to experimental H₂ yields between 21.1 wt% and 26.3 wt% and equilibrium H₂ yields between 27.3 and 29.4 wt% at 600 and 800 °C, themselves significantly lower than the theoretical maximum of 37 wt%. The H₂ yield efficiencies were mirrored by the steam conversion efficiency (H₂O conv (eff)), which peaked at 77%, making clear that the hydrogen produced originated from reaction with water through SR and water gas shift, although on the basis of Fig. 5 alone, the water gas shift contribution was not identifiable. Reforming efficiency followed the same trends. Selectivity to hydrogen increased from 95% to 99.8% between 600 and 800 °C.

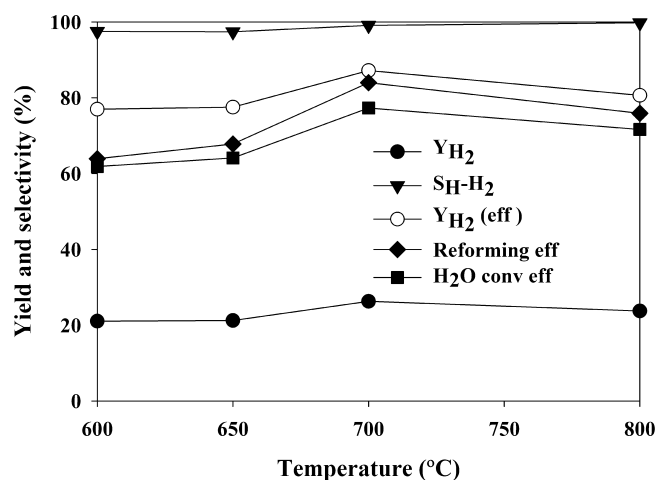


Fig. 5. Effect of temperature on Y_{H₂} (wt%) and S_{H-H₂} (%) using Ni/Al catalysts at S/C of 3 and WHSV of 3.52 h⁻¹ with biodiesel and water vaporiser temperatures set to 365 and 170 °C respectively.

Overall these main outputs indicated that hydrogen production during the initial stages of CSR of biodiesel, as reflected in the duration of the experiments, is possible with decent hydrogen yield and high selectivity. The reasons for hydrogen yield efficiencies below 100% are explored below by considering the feedstock conversion

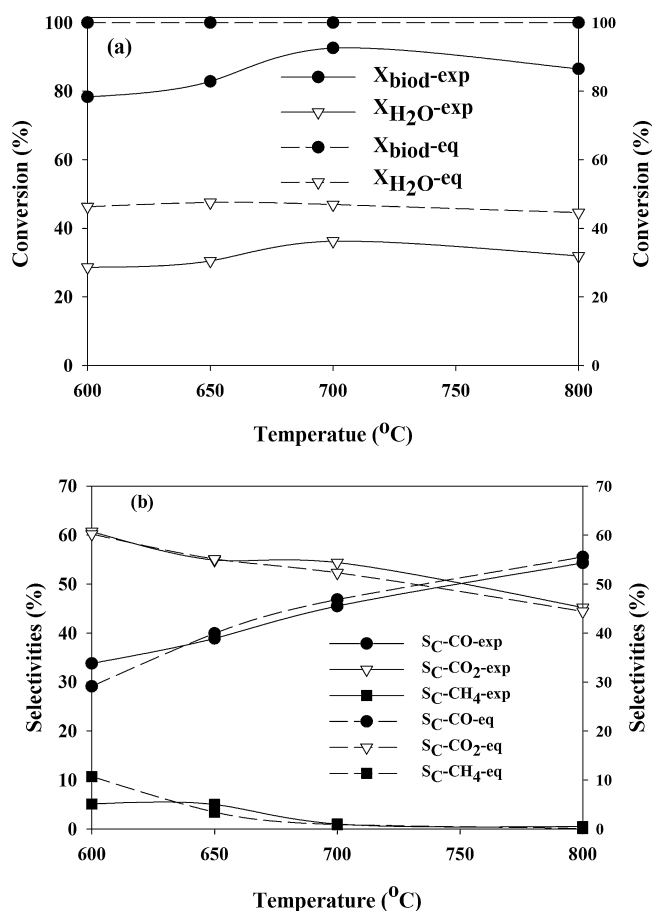


Fig. 6. Effect of temperature on biodiesel CSR (a) (X_{biod}) (X_{H_2O}), and (b) (S_C) using same conditions as Fig. 5.

to the desirable gases CO_2 , and to a smaller extent CO as indicator of changing water gas shift contribution, and to the unwanted by-products such as CH_4 , C_2 – C_4 gases, carbon on the catalyst, and carbon in condensates. These are shown in Fig. 6a, which plots the fuel (X_{biod}) and steam conversions (X_{H_2O}), Fig. 6b with the selectivity to carbon gases, including equilibrium values, and Table 4, which lists the individual contributions (gas/condensate/catalyst) to the carbon balance.

In Table 4, the carbon balance does not include carbon deposited on parts other than the catalyst, e.g., reactor walls, feeding lines, the difficulty residing in collecting thin layers of this carbonaceous residue in inaccessible sections of the experimental set up. This partly explains why the molar carbon balance $100 \times (1 - C_{out}/C_{in})$ was in some cases within 12–13 mol% of the carbon feed rather than the desired range below 5 mol%. It is assumed that poor closure of the carbon balance was contributed by conditions where coke deposited on parts other than the catalyst via homogeneous thermal decomposition reactions prior to reaching the catalytic active sites.

Although equilibrium conditions predicted complete biodiesel conversion, the experimental conversion of biodiesel to gas phase carbon products (X_{biod}) exhibited a rise from 80% at 600 °C to 92% at 700 °C, and upon further temperature increase, it decreased slightly, with similar observations made for steam conversion (28–33%) (Fig. 6a).

Lowest conversion of biodiesel to gas phase carbon products (X_{biod}) was observed at 600 °C (Fig. 6a) as a result of higher carbon formation on the catalyst surface due to decomposition reaction. This is expressed by carbon on the catalyst equivalent to 16% of C_{out} , the total carbon measured in the products (Table 4). For this

run, 6% of the carbon feed were unaccounted for, which were most likely coke generated elsewhere in the set up. In terms of utilization of the biodiesel, the 600 °C condition reflected three pathways: [i] non-catalytic thermal decomposition (R-3), [ii] catalytic thermal decomposition (R-3) and Boudouard (R-6), and [iii] SR (R-1). The first two would have caused lower H_2 yield due to non-conversion of the steam reactant. The low steam conversion of 28.6%, equivalent to just 62% efficiency at 600 °C supports this interpretation. Formation of small amount of alkenes i.e., C_2H_4 was detected at this temperature, which is a known soot precursor [55]. A small amount of C_2H_6 was also discovered, which, along with CH_4 , further impacted on hydrogen yield and selectivity. Carbon on the catalyst at 650 °C was lower compared to 600 °C, accounting for just 4% of C_{out} (Table 4). This was likely due to the reverse Boudouard reaction (rev R-6), affecting accordingly the selectivity to CO and to CO_2 (Fig. 6b).

At 700 °C, the temperature of highest H_2 yield efficiency (87%), biodiesel and steam conversions increased under combined effects of increase in SR (R-1), SMR (R-5), and decomposition reaction (R-3). The carbon balance for 700 °C was near zero, while the carbon in the condensates was negligible, indicating the products were gases CO , CO_2 , CH_4 and some coke on the catalyst (7% of C_{out}). This implied the fuel conversion was now predominantly consisting of catalytic reactions (SR i.e., R-1), SMR (rev R-5), thermal decomposition (R-3), but no longer non catalytic thermal decomposition. This can be explained by faster kinetics of (R-1) which would have deprived (R-3) of biodiesel reactant. Increase in hydrogen yield (Fig. 5) along with selectivity to H_2 and CO (Figs. 5 and 6b) support the hypothesis. Selectivity to methane decreased with increasing temperature, following equilibrium trends which were adverse to the methanation reaction (R-5) and favourable to SMR (rev R-5). Highest biodiesel and steam conversions of 96.3% and 36.3% at 700 °C (Fig. 6a) resulted in the highest hydrogen yield efficiency recorded in these experiments. At similar S/C of 2.5 and 700 °C with WHSV of 1.967 h^{-1} , Pimenidou et al. [11] reported lower fuel (waste cooking oil) and steam conversions i.e., 86.3% and 35.7%, respectively. Finally at 800 °C, both biodiesel and steam conversions declined, lowering the hydrogen yield. High temperature promoted reverse water gas shift reaction (rev R-2) limiting the conversion of H_2O to H_2 (Fig. 6a) leaving some CO unreacted. However, the H_2 yield efficiency also decreased between 700 and 800 °C from 87.2% to 80.6% (Fig. 5), suggesting conditions moving further away from equilibrium than at 700 °C. As a temperature rise favors the kinetics of the reactions at work, this drop in H_2 yield (eff) reflected a deactivation of the catalyst. This could be caused by loss of surface area and to sintering of Ni crystallites as listed in Table 3. Although the yield of hydrogen at 800 °C was lower compared to 700 °C, 99.8% hydrogen selectivity was observed as result of negligible selectivity to methane, in agreement with equilibrium trend. The lower yield of hydrogen is here explained by a lower catalytic activity which then re-opens the competing biodiesel conversion path to non-catalytic thermal decomposition (R-3), evidenced by the poor carbon balance closure (12%) in spite of little carbon deposition on the catalyst (1% of C_{out} , Table 4).

To summarize the effects of temperature, 600 °C sees lower hydrogen yield and selectivity caused by catalytic thermal decomposition and Boudouard reactions resulting in coke in the reactor and on the catalyst alongside with methanation. At 650 °C, methanation decreases but non catalytic decomposition increases (poor balance closure), at the same time, reverse Boudouard reaction eliminates carbon on the catalyst. At 700 °C, SR is at its most active, mitigated by some reverse water gas shift, dominating over the unwanted pathways of decomposition (good balance closure). At 800 °C, the catalyst shows signs of deactivation in a context of stronger reverse water gas shift, re-opening the path of biodiesel conversion to non catalytic thermal decomposition yielding carbon

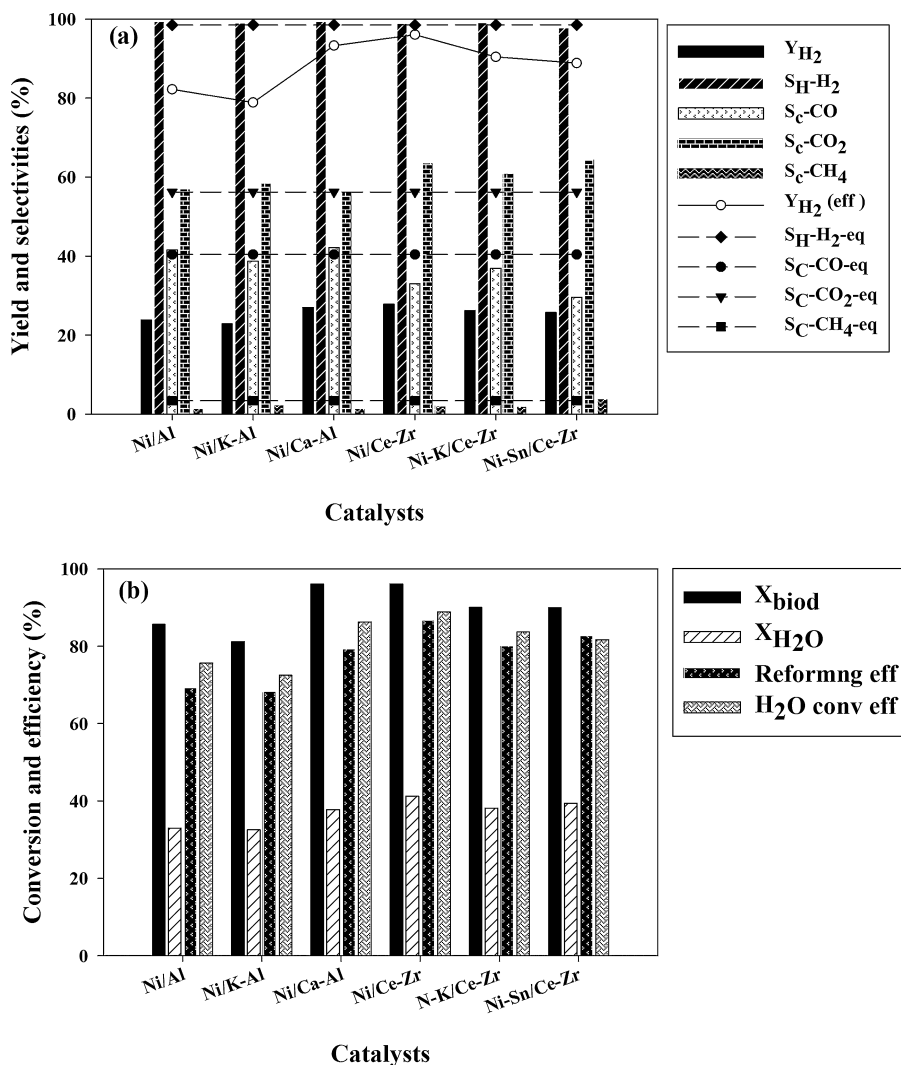


Fig. 7. Catalytic performance of Ni supported on Al_2O_3 and Ce-Zr catalysts (a) Y_{H_2} (wt%), Y_{H_2} (eff) and (S_H and S_C), and (b) (X_{biod}) and (X_{H_2O}), steam (H_2O conv eff) and reforming efficiency, in CSR of biodiesel at S/C of 3 and WHSV of $3.18\ h^{-1}$ using 190 and 170 °C as biodiesel and water vaporiser temperatures.

and hydrogen products. However for this catalyst, carbon deposition remained an issue, as 7% of C_{out} was still measured for the temperature with the highest H_2 yield efficiency (700 °C, 87% H_2 yield eff).

3.3.2. Effect of catalyst

Zhu [56] found that pyrolysis of biodiesel began above 350 °C. According to our TGA results on biodiesel samples under nitrogen flow, biodiesel starts vapourizing around 190 °C (Supplement 5), evidenced by a large gradient of mass loss. To prevent our biodiesel feedstock from undergoing pyrolysis prior to contacting the catalyst while maximizing feedstock conversion by CSR, the vaporiser temperature was lowered to 190 °C to evaluate the effect of catalyst characteristics on the efficiency of the hydrogen production. The effect of catalyst on the CSR processes was examined at S/C of 3 at 650 °C using 190 and 170 °C as vaporiser temperatures for biodiesel and water respectively at a WHSV of $3.18\ h^{-1}$ with constant carbon feed rate of $1.50 \times 10^{-5}\ mol\ s^{-1}$. According to XRD and BET results, the smallest crystallite size and highest surface area was exhibited by the Ni supported on pre-calcined Ce-Zr prepared by wet impregnation, hence this catalyst was selected for the evaluation. Similarly, the doped catalysts were prepared by the same method using the pre-calcined Ce-Zr support. The Ce-Zr supported catalysts were mixed with quartz sand particles of 150–200 μm size

in a mass ratio of 75:25 to make up 2.0506 g of reactor load. The catalyst was sandwiched between two quartz wool plugs (4 μm diameter fiber).

See Excel sheet 1 as supplementary file. Supplementary material related to this article found, in the online version, at <http://dx.doi.org/10.1016/j.apcath.2014.12.010>.

The performance of the catalysts in terms of hydrogen yield was as follows: Ni/Ce-Zr \geq Ni/Ca-Al > Ni-Sn/Ce-Zr > Ni-K/Ce-Zr > Ni/Al > Ni-K/Al (Fig. 7a). Highest hydrogen yields of 27.8 wt% and 27.0 wt%, representing yield efficiencies of 93.5% and 91%, were obtained for the Ni/Ce-Zr and the Ni/Ca-Al, respectively. These were accompanied by highest biodiesel reforming and steam conversion efficiencies among all the catalysts (Fig. 7b). Hydrogen selectivity for all the catalysts was above 97% (Fig. 7a). In CSR of palm fatty acid distillate (PFAD) using Rh and Ni supported on $Ce_{0.75}Zr_{0.25}O_2$ selectivity to hydrogen of 70 and 56.7% were reported by Laosiripojana et al. [57] and Shotipruk et al. [58] using S/C of 3 at 800 and 900 °C, respectively.

Biodiesel conversions (X_{biod}) of 96.0% and 96.1% with 37.8% and 41.3% steam conversions (X_{H_2O}) were obtained with Ca-Al and Ce-Zr supported catalysts, respectively. Vagia and Lemonidou [59] reported the benefits of using calcium aluminate supported SR catalysts. They found that Ni was distributed at the boundaries of the grains facilitating the high degree of dispersion. Further, the smaller

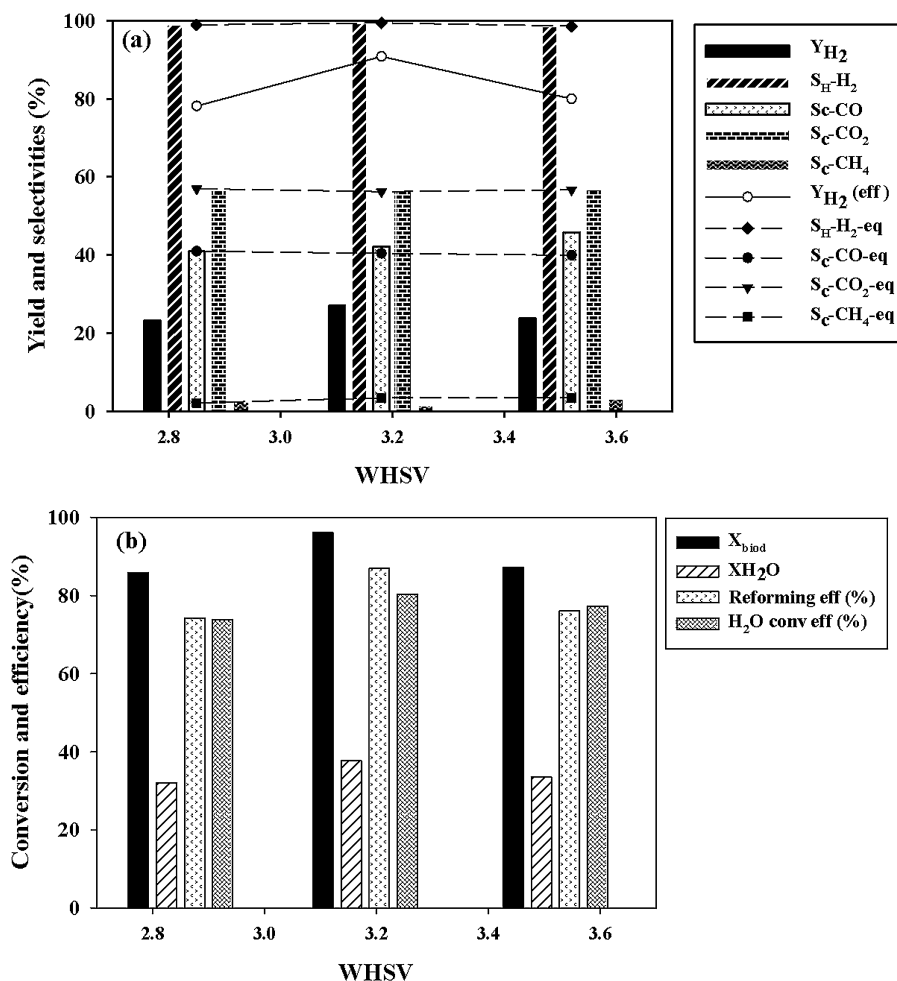


Fig. 8. Effect of WHSV on the performance of CSR of biodiesel (a) Y_{H_2} (wt%), Y_{H_2} (eff), and (S_H and S_C), and (b) (X_{biod}) and (X_{H_2O}), (H_2O conv eff) and reforming efficiency, using Ni/Ca–Al catalyst at 650 °C with S/C of 3.0 and WHSV of 3.18 h^{−1}. The biodiesel and water vaporisers for this evaluation were set to 190 and 170 °C, respectively.

crystallites of Ni over the support contributed to the difference in dispersion and caused high reforming activity. The presence of Ca in the case of calcium aluminate based catalyst has shown to influence the performance of the catalyst [60]. Formation of less crystalline carbon was observed in Ca modified catalysts which were more easily gasified (R-4) during the CSR reaction. Addition of Ca decreased the acidity of the Al_2O_3 and increased the adsorption of steam while providing the Ni catalyst the proximity and abundance of adsorbed OH groups affecting the performance of the catalyst [61].

In the case of Ce–Zr based catalyst, the presence of Ce has been found to result in higher conversion and water gas shift activity [62]. Ce addition is well known to promote metal activity and dispersion, resulting in high catalytic activity (Table 2). Similarly the presence of Ce increases adsorption of steam thereby promoting steam conversion. Higher CO_2 selectivity and steam conversion during the CSR reaction suggested higher water gas shift reaction (R-2) activity. It was reported that CeO_x enhances the dissociation of H_2O and accelerates the reaction of steam with adsorbed species on the nickel surface near the boundary area between metal and support, thus decreasing the carbon deposition (as seen in Table 4) and promoting the stability of the catalyst during reforming [63]. Higher surface area for both catalysts (Ni/Ca–Al and Ni/Ce–Zr) compared to Al_2O_3 alone supported catalyst (Ni/Al and Ni–K/Al) could also be one of the reasons for higher catalytic activity, as in [64].

Biodiesel conversion decreased by 5% over Ni–K/Al catalyst relatively to Ni/Al (Fig. 7b). Addition of K to Al_2O_3 catalysts here reduced catalytic activity of Ni/Al catalyst. As steam adsorption

increases due to addition of K, steam conversion remained unaffected. Borowiecki et al. [65] reported that addition of potassium in SMR reduces the formation of CH_x fragments on the nickel surface and increased steam adsorption on the catalyst surface resulting in lower catalytic activity.

Likewise in case of Ni–K/Ce–Zr, biodiesel and steam conversion decreased by 6% and 5% relatively to Ni/Ce–Zr. The decrease in biodiesel and steam conversion with Ni–K/Ce–Zr can be the result of higher carbon formation on the catalyst surface (Table 4) or sintering of Ni crystallites (Table 3). Supplement 4 shows the SEM image of used Ni–K/Ce–Zr catalyst tested at the same conditions tested at the same conditions mentioned in the Fig. 7. It can be seen that the catalyst surface is covered with carbon and formation of carbon nano tubes was observed over the catalyst surface. In all the three Ni/Ce–Zr, Ni–K/Ce–Zr and Ni–Sn/Ce–Zr catalysts, Ni–K/Ce–Zr catalyst showed the highest carbon formation.

See Excel sheet 1 as supplementary file. Supplementary material related to this article found, in the online version, at <http://dx.doi.org/10.1016/j.apcatb.2014.12.010>.

It was hoped that addition of K would reduce carbon formation, but this ability of the catalyst is dependent on the position and amount of K on the catalyst surface. According to Borowiecki et al. [32] location of K on the catalyst plays an important role in resistance of K containing catalyst to carbon formation. A part of K is in an intimate contact with nickel, whereas the other part is distributed over the support. In catalyst where K–Ni interaction dominates, K promoted catalyst exhibits lower resistance to

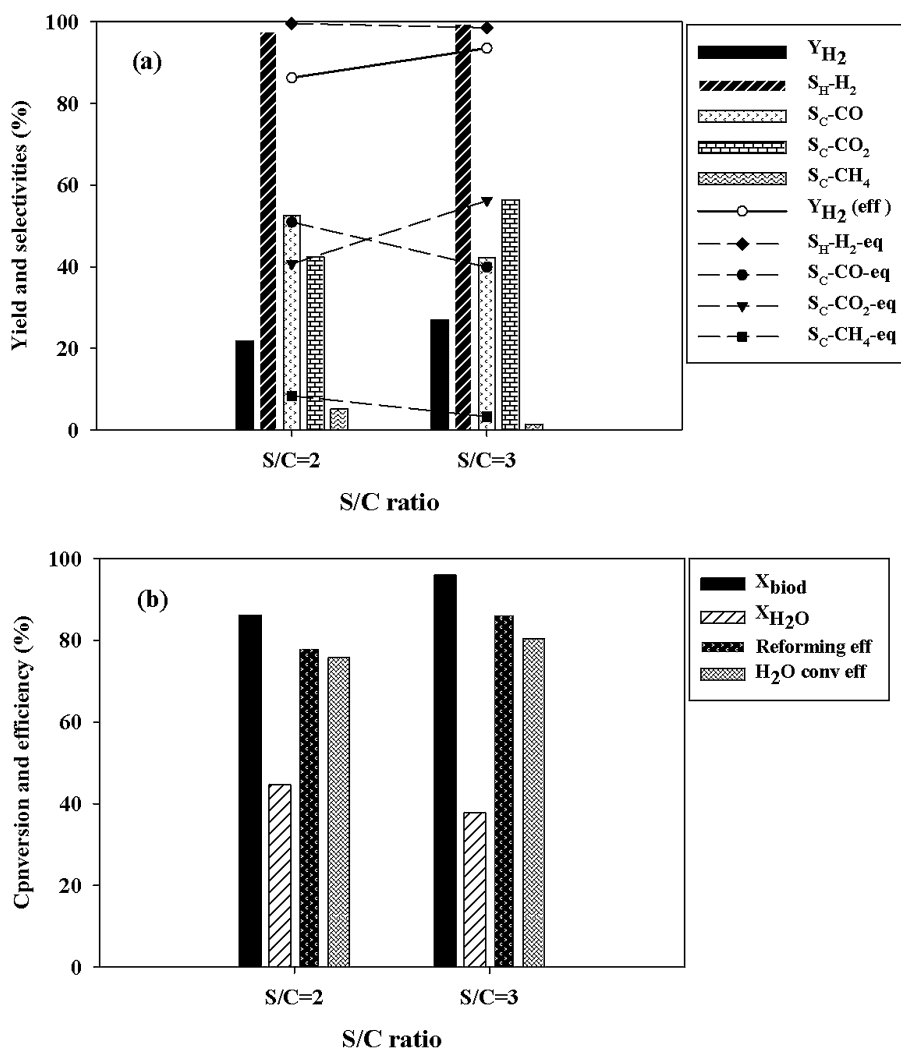


Fig. 9. Effect of S/C molar ratio on the performance of CSR of biodiesel using Ni/Ca–Al (a) Y_{H_2} (wt%), Y_{H_2} (eff) and (S_C and S_H), (b) (X_{biod}) and (X_{H_2O}), (H_2O conv eff) and reforming efficiency, using Ni/Ca–Al catalyst at 650 °C and WHSV of 3.18 h^{−1} using 190 and 170 °C as biodiesel and water vaporiser temperatures.

carbon formation. Further decreased surface area of the catalyst in our evaluations could also be one of the reasons for lower activity of the catalyst.

Biodiesel and steam conversions of 90.0% and 39.4% were measured over Ni–Sn/Ce–Zr catalyst (Fig. 7b). Reduction in the catalytic activity compared to Ni/Ce–Zr, could be as a result of surface coverage of active Ni sites by Sn reducing the activity of the catalyst [40]. Similar behavior was reported by Nikolla et al. [66] in SMR using S/C of 0.5 at 800 °C using Ni/YSZ catalyst. Addition of Sn was reported to increase the stability of the catalyst but was shown to reduce activity; a 25% decrease in the activity was reported with 5 wt% Sn doped Ni/YSZ catalyst. Formation of relatively higher amount of carbon on the surface of Ni–Sn/Ce–Zr compared to Ni/Ce–Zr could be one of the reasons for lower activity of the catalyst, resulting from formation of alkenes [55].

In general, selectivity to carbon gases was very close to equilibrium. Alumina based catalysts i.e., Ni/Al, Ni–K/Al and Ni/Ca–Al showed higher CO and lower CO₂ selectivity compared to the Ce–Zr supported catalysts (Ni/Ce–Zr, Ni–K/Ce–Zr and Ni–Sn/Ce–Zr). This could be as a result of lower water gas shift activity of the Al₂O₃ supported catalyst in comparison to Ce–Zr ones. Addition of K to the catalysts (Ni/Al and Ni/Ce–Zr) slightly increased selectivity to CH₄. According to Meeyoo et al. [67] addition of K to the catalyst is shown to decrease methane activation on Ni sites, thus decreasing

SMR (R-5) activity and resulting in higher selectivity to CH₄. Selectivity to CH₄ was highest over Ni–Sn/Ce–Zr among all the catalysts examined.

Formation of alkenes like C₂H₄ and C₃H₆ observed for the Ni/Ce–Zr and Ni–Sn/Ce–Zr catalysts were very similar. Addition of K to the catalyst was shown to prevent the formation of alkenes over Ce–Zr supported catalysts. The Ce–Zr supported catalyst showed relatively small amount of unaccounted carbon as compared to other catalysts examined.

3.3.3. Effect of reaction time and molar steam to carbon ratio

To study the effect of reaction time, represented by the inverse of the WHSV, and of S/C on the performance of the CSR of biodiesel, the Ni/Ca–Al was selected for the evaluation because it had one of the best efficiencies of H₂ yield of all the catalysts studied. The effect of WHSV was studied using S/C of 3 at 650 °C and is shown in Fig. 8. Maximum conversions of both biodiesel and steam and therefore H₂ yield (27 wt%) were observed at 3.18 h^{−1}, with very good mass balance closure (Table 4). Increase in WHSV increased the amount of carbon in the condensate as observed by CHN–O analysis (Table 4) which could suggest increased pyrolysis of biodiesel.

The effect of S/C ratio on the performance of Ni/Ca–Al in CSR of biodiesel at WHSV of 3.18 h^{−1} and 650 °C is represented in Fig. 9. Fuel conversion increased with S/C following Le

Chatelier's principle, while, as expected from conditions of excess steam, steam conversion decreased. Near stoichiometric steam conditions ($S/C=2$) resulted in higher formation of carbonaceous deposits and biodiesel cracking products (Table 4), resulting in lower hydrogen yield compared to $S/C=3$. Similarly to all the experiments, the selectivity to individual gases was very close to the equivalent equilibrium value.

4. Conclusion

Hydrogen can be successfully produced via catalytic steam reforming of biodiesel. Effect of S/C , temperature, WHSV, catalyst and biodiesel characteristics on the early H_2 yield and other process outputs such as carbon deposition on the catalyst was examined over the first 2 h of steady state operation. Ni supported on Ca–Al and on Ce–Zr supported catalysts exhibited the best performances, with H_2 yield efficiencies of 91% and 94%, respectively, at reformer temperature 650 °C, WHSV of 3.18 h⁻¹, S/C of 3, with biodiesel pre-heat temperature of 190 °C, i.e., just under biodiesel vaporization point, which suppressed non catalytic thermal decomposition prior to CSR. Carbon deposition on the catalyst represented 3.6% and 1.3% of the carbon feed in these conditions for the Ni/Ca–Al and the Ni/Ce–Zr catalysts, respectively. Longer runs of the order of at least 100 h would be required to obtain more realistic steady state carbon deposition data, as this tends to vary in the early period of industrial catalyst life. Addition of dopants like K and Sn had a negative effect on the H_2 yield. Increase in S/C from near stoichiometric to moderate excess of steam conditions had the expected positive effect on the process performance (biodiesel and steam conversion) thus improving hydrogen yield.

Acknowledgments

The following are gratefully acknowledged: RCUK for consumables support through grant EP/G01244X/1 (Supergen XIV 'Delivery of Sustainable Hydrogen'), Jim Abbott at Johnson Matthey for the Ni/Al catalyst, MEL chemicals and TST Ltd., for catalytic materials and supports, Robert Bloom, Zaheer Abbas and Oluwafemi Omoniye for assistance in the lab, Feng Cheng for initial help with CEA modelling and valuable discussions.

References

- [1] Nations U. World Population Prospects, 2012 [cited; Available from: <http://esa.un.org/unpd/wpp/unpp/panel.population.htm>
- [2] K. Hall, 4.14 – Future Perspective on Hydrogen and Fuel Cells, in: *Comprehensive Renewable Energy*, in: A. Sayigh (Ed.), Elsevier, Oxford, 2012, pp. 351–360.
- [3] C.J. Dawson, J. Hilton, Fertiliser availability in a resource-limited world: production and recycling of nitrogen and phosphorus, *Food Policy* 36 (2011) S14–S22.
- [4] S. Angel, Global Hydrogen Growth Investor Day, PRAXAIR, 2011, pp. 47.
- [5] P.P. Edwards, et al., Hydrogen and fuel cells: towards a sustainable energy future, *Energy Policy* 36 (12) (2008) 4356–4362.
- [6] M. Marquievich, et al., Hydrogen production by steam reforming of vegetable oils using nickel-based catalysts, *Ind. Eng. Chem. Res.* 40 (22) (2001) 4757–4766.
- [7] M. Marquievich, F. Medina, D. Montané, Hydrogen production via steam reforming of sunflower oil over Ni/Al catalysts from hydrotalcite materials, *Catal. Commun.* 2 (3–4) (2001) 119–124.
- [8] M. Marquievich, R. Coll, D. Montané, Steam reforming of sunflower oil for hydrogen production, *Ind. Eng. Chem. Res.* 39 (7) (2000) 2140–2147.
- [9] M. Marquievich, R. Coll, D. Montané, Steam reforming of sunflower oil for hydrogen production, *Ind. Eng. Chem. Res.* 39 (7) (2000) 2632.
- [10] S. Jain, M.P. Sharma, Kinetics of acid base catalyzed transesterification of *Jatropha curcas* oil, *Bioresour. Technol.* 101 (20) (2010) 7701–7706.
- [11] P. Pimenidou, et al., Chemical looping reforming of waste cooking oil in packed bed reactor, *Bioresour. Technol.* 101 (16) (2010) 6389–6397.
- [12] P. Pimenidou, et al., High purity H_2 by sorption-enhanced chemical looping reforming of waste cooking oil in a packed bed reactor, *Bioresour. Technol.* 101 (23) (2010) 9279–9286.
- [13] A. Shotipruk, et al., Reactivity of and toward steam reforming of palm fatty acid distilled (PFAD) with co-fed oxygen and hydrogen, *Chem. Eng. Sci.* 64 (3) (2009) 459–466.
- [14] R.M. Zin, et al., High hydrogen yield and purity from palm empty fruit bunch and pine pyrolysis oils, *Int. J. Hydrogen Energy* 37 (14) (2012) 10627–10638.
- [15] S. Wang, et al., Hydrogen production via catalytic reforming of the bio-oil model compounds: acetic acid, phenol and hydroxyacetone, *Int. J. Hydrogen Energy* 0 (2014).
- [16] R. Trane, et al., Catalytic steam reforming of bio-oil, *Int. J. Hydrogen Energy* 37 (8) (2012) 6447–6472.
- [17] V. Dupont, et al., Thermodynamics of hydrogen production from urea by steam reforming with and without in situ carbon dioxide sorption, *Int. J. Hydrogen Energy* 38 (25) (2013) 10260–10269.
- [18] A.N. Rollinson, et al., Hydrogen from urea–water and ammonia–water solutions, *Appl. Catal. B: Environ.* 106 (3–4) (2011) 304–315.
- [19] G.J. Kraaij, et al., Biodiesel fuel processor for APU applications, *Int. J. Hydrogen Energy* 34 (10) (2009) 4495–4499.
- [20] S. Martin, A. Wörner, On-board reforming of biodiesel and bioethanol for high temperature PEM fuel cells: comparison of autothermal reforming and steam reforming, *J. Power Sources* 196 (6) (2011) 3163–3171.
- [21] G.A. Nahar, Hydrogen rich gas production by the autothermal reforming of biodiesel (FAME) for utilization in the solid-oxide fuel cells: a thermodynamic analysis, *Int. J. Hydrogen Energy* 35 (17) (2010) 8891–8911.
- [22] S. Martin, et al., An experimental investigation of biodiesel steam reforming, *Int. J. Hydrogen Energy* 40 (1) (2014) 95–105.
- [23] J. Lin, et al., Bio-fuel reforming for solid oxide fuel cell applications. Part 2: biodiesel, *Int. J. Hydrogen Energy* 39 (1) (2014) 183–195.
- [24] Y. Shiratori, et al., Paper-structured catalyst for the steam reforming of biodiesel fuel, *Int. J. Hydrogen Energy* 38 (26) (2013) 11278–11287.
- [25] G. Nahar, K. Kendall, Biodiesel formulations as fuel for internally reforming solid oxide fuel cell, *Fuel Process. Technol.* 92 (7) (2011) 1345–1354.
- [26] Y. Shiratori, T. Quang-Tuyen, K. Sasaki, Performance enhancement of biodiesel fueled SOFC using paper-structured catalyst, *Int. J. Hydrogen Energy* 38 (23) (2013) 9856–9866.
- [27] T. Quang-Tuyen, Y. Shiratori, K. Sasaki, Feasibility of palm-biodiesel fuel for a direct internal reforming solid oxide fuel cell, *Int. J. Energy Research* 37 (6) (2013) 609–616.
- [28] Z.F. Zhou, et al., Direct oxidation of waste vegetable oil in solid-oxide fuel cells, *J. Power Sources* 171 (2) (2007) 856–860.
- [29] J. Xuan, et al., A review of biomass-derived fuel processors for fuel cell systems, *Renewable Sustainable Energy Rev.* 13 (6–7) (2009) 1301–1313.
- [30] A.F. Demba Diop, S. Michel, K. Magdalena Anna, M. Martin Mautner, 2013, Assessing the impact of biofuels production on developing countries from the point of view of Policy Coherence for Development, The European Union's Framework Contract Commission 2011, p168.
- [31] J. Lin, C.W. Babbitt, T.A. Trabbold, Life cycle assessment integrated with thermodynamic analysis of bio-fuel options for solid oxide fuel cells, *Bioresour. Technol.* 128 (0) (2013) 495–504.
- [32] T. Borowiecki, et al., Studies of potassium-promoted nickel catalysts for methane steam reforming: effect of surface potassium location, *Appl. Surf. Sci.* 300 (0) (2014) 191–200.
- [33] G. Nahar, V. Dupont, Hydrogen via steam reforming of liquid biofeedstock, *Biofuels* 3 (2) (2012) 167–191.
- [34] D.L. Trimm, Catalysts for the control of coking during steam reforming, *Catal. Today* 49 (1–3) (1999) 3–10.
- [35] J. Sehested, Four challenges for nickel steam-reforming catalysts, *Catal. Today* 111 (1–2) (2006) 103–110.
- [36] D.L. Trimm, Coke formation and minimisation during steam reforming reactions, *Catal. Today* 37 (3) (1997) 233–238.
- [37] F. Mariño, et al., Cu–Ni–K/(–Al₂O₃) supported catalysts for ethanol steam reforming: formation of hydrotalcite-type compounds as a result of metal – support interaction, *Appl. Catal. A: Gen.* 238 (1) (2003) 41–54.
- [38] Y. Zhang, et al., Potassium catalytic hydrogen production in sorption enhanced gasification of biomass with steam, *Int. J. Hydrogen Energy* 39 (9) (2014) 4234–4243.
- [39] I. Alstrup, et al., 1998. Promotion of steam reforming catalysts, in *Studies in Surface Science and Catalysis*, D.S.F.F.A.V.A. Parmaliana, A.F., (Ed.), Elsevier, 5–14.
- [40] S. Pengpanich, et al., iso-Octane partial oxidation over Ni–Sn/CeO₂. 75ZrO₂. 25O₂ catalysts, *Catal. Today* 136 (3–4) (2008) 214–221.
- [41] S. Bernal, et al., Some recent results on metal/support interaction effects in Ni/CeO₂ (NM: noble metal) catalysts, *Catal. Today* 50 (2) (1999) 175–206.
- [42] Y. Nagai, et al., X-ray absorption fine structure analysis of local structure of CeO₂–ZrO₂ mixed oxides with the same composition ratio (Ce/Zr = 1), *Catal. Today* 74 (3–4) (2002) 225–234.
- [43] L.F. Liotta, et al., Effects of redox treatments on the structural composition of ceria–zirconia oxide for application in the three-way catalysis, *Appl. Catal. A: Gen.* 240 (1–2) (2003) 295–307.
- [44] M. Kuhn, et al., Structural characterization and oxygen nonstoichiometry of ceria–zirconia (Ce_{1-x}Zr_xO_{2-y}) solid solutions, *Acta Mater.* 61 (11) (2013) 4277–4288.
- [45] Z. Yang, T.K. Woo, K. Hermansson, Effects of Zr doping on stoichiometric and reduced ceria: a first-principles study, *J. Chem. Phys.* 124 (22) (2006).
- [46] G. Nahar, V. Dupont, Hydrogen production from simple alkanes and oxygenated hydrocarbons over ceria–zirconia supported catalysts: review, *Renewable Sustainable Energy Rev.* 32 (0) (2014) 777–796.

- [47] A. Osmont, L. Catoire, I. Gökalp, Thermochemistry of methyl and ethyl esters from vegetable oils, *Int. J. Chem. Kinet.* 39 (9) (2007) 481–491.
- [48] L.B. McCusker, et al., Rietveld refinement guidelines, *J. Appl. Crystallography* 32 (1) (1999) 36–50.
- [49] P. Biswas, D. Kunzru, Steam reforming of ethanol for production of hydrogen over Ni/CeO–ZrO catalyst: effect of support and metal loading, *Int. J. Hydrogen Energy* 32 (8) (2007) 969–980.
- [50] A. Siahvashi, A.A. Adesina, Synthesis gas production via propane dry (CO₂) reforming: influence of potassium promotion on bimetallic Mo–Ni/Al₂O₃, *Catal. Today* 214 (0) (2013) 30–41.
- [51] F. Cheng, V. Dupont, Nickel catalyst auto-reduction during steam reforming of bio-oil model compound acetic acid, *Int. J. Hydrogen Energy* 38 (35) (2013) 15160–15172.
- [52] H. Chen, et al., A novel mesostructured alumina–ceria–zirconia tri-component nanocomposite with high thermal stability and its three-way catalysis, *Microporous and Mesoporous Mater.* 143 (2–3) (2011) 368–374.
- [53] K. Aasberg-Petersen, et al., Technologies for large-scale gas conversion, *Appl. Catal. A: Gen.* 221 (1–2) (2001) 379–387.
- [54] T. Sukonket, et al., Influence of the catalyst preparation method, surfactant amount, and steam on CO₂ Reforming of CH₄ over 5Ni/CeO. 6ZrO. 4O₂ catalysts, *Energy Fuels* 25 (3) (2011) 864–877.
- [55] S. Yoon, I. Kang, J. Bae, Effects of ethylene on carbon formation in diesel autothermal reforming, *Int. J. Hydrogen Energy* 33 (18) (2008) 4780–4788.
- [56] Y. Yhu, 2012 An Experimental Study on Thermal Stability of Biodiesel Fuel, in *Biomedical and Chemical Engineering*, L.C. Smith College of Engineering and Computer Science: Surface. p. 144.
- [57] N. Laosiripojana, et al., Effects of support and co-fed elements on steam reforming of palm fatty acid distillate (PFAD) over Rh-based catalysts, *Appl. Catal. A: Gen.* 383 (1–2) (2010) 50–57.
- [58] A. Shotipruk, et al., Reactivity of CeO₂ and Ce–ZrO₂ toward steam reforming of palm fatty acid distilled (PFAD) with co-fed oxygen and hydrogen, *Chem. Eng. Sci.* 64 (3) (2009) 459–466.
- [59] E.C. Vagia, A.A. Lemonidou, Hydrogen production via steam reforming of bio-oil components over calcium aluminate supported nickel and noble metal catalysts, *Appl. Catal. A: Gen.* 351 (1) (2008) 111–121.
- [60] C.K.S. Choong, et al., Effect of calcium addition on catalytic ethanol steam reforming of Ni/Al₂O₃: I catalytic stability, electronic properties and coking mechanism, *Appl. Catal. A: Gen.* 407 (1–2) (2011) 145–154.
- [61] C.K.S. Choong, et al., Effect of calcium addition on catalytic ethanol steam reforming of Ni/Al₂O₃: II acidity/basicity, water adsorption and catalytic activity, *Appl. Catal. A: Gen.* 407 (1–2) (2011) 155–162.
- [62] S. Hilaire, et al., A comparative study of water–gas–shift reaction over ceria-supported metallic catalysts, *Appl. Catal. A: Gen.* 258 (2) (2004) 271–276.
- [63] W.-S. Dong, et al., Methane reforming over Ni/Ce–ZrO₂ catalysts: effect of nickel content, *Appl. Catal. A: Gen.* 226 (1–2) (2002) 63–72.
- [64] N. Laosiripojana, S. Assabumrungrat, Catalytic steam reforming of ethanol over high surface area CeO₂: the role of CeO₂ as an internal pre-reforming catalyst, *Appl. Catal. B: Environ.* 66 (1–2) (2006) 29–39.
- [65] T. Borowiecki, W. Gac, A. Denis, Effects of small MoO₃ additions on the properties of nickel catalysts for the steam reforming of hydrocarbons: III. reduction of Ni–Mo/Al₂O₃ catalysts, *Appl. Catal. A: Gen.* 270 (1–2) (2004) 27–36.
- [66] E. Nikolla, J. Schwank, S. Linic, Promotion of the long-term stability of reforming Ni catalysts by surface alloying, *J. Catal.* 250 (1) (2007) 85–93.
- [67] V., Meeyoo, et al. Steam reforming of ethanol over Ni/Ce_{0.75}Zr_{0.25}O₂ and Ni–K/Ce_{0.75}Zr_{0.25}O₂ catalysts, in *Chemeca 2011 (39th): 2011: Sydney, N.S.W.*, 2011, Engineers Australia: Barton, A.C.T. p. [807–816].